

# MicroScopiQ: Accelerating Foundational Models through Outlier-Aware Microscaling Quantization

Akshat Ramachandran  
Georgia Institute of Technology  
Atlanta, GA  
akshat.r@gatech.edu

Souvik Kundu  
Intel Labs  
San Diego, CA  
souvik.kundu@intel.com

Tushar Krishna  
Georgia Institute of Technology  
Atlanta, GA  
tushar@ece.gatech.edu

## Abstract

Quantization of foundational models (FMs) is significantly more challenging than traditional DNNs due to the emergence of large magnitude values called outliers. Existing outlier-aware algorithm-architecture co-design techniques either use mixed-precision, retaining outliers at high precision but compromise hardware efficiency, or quantize inliers and outliers at the same precision, improving hardware efficiency at the cost of accuracy. To address this mutual exclusivity, in this paper, we propose MicroScopiQ, a novel co-design technique that leverages pruning to complement outlier-aware quantization. MicroScopiQ retains outliers at higher precision while pruning a certain fraction of least important weights to distribute the additional outlier bits; ensuring high accuracy, aligned memory and hardware efficiency. We design a high-throughput, low overhead accelerator architecture composed of simple multi-precision INT processing elements and a novel network-on-chip called ReCoN that efficiently abstracts the complexity of supporting high-precision outliers. Additionally, unlike existing alternatives, MicroScopiQ does not assume any locality of outlier weights, enabling applicability to a broad range of FMs. Extensive experiments across various quantization settings show that MicroScopiQ achieves SoTA quantization performance while simultaneously improving inference performance by 3× and reducing energy by 2× over existing alternatives.

## 1 Introduction

Recent advancements in AI [2, 21, 40, 73] are propelled by a class of models called foundational models (FMs), including large language models (LLMs) and vision-language models (VLMs). FMs leverage billion-scale parameters for improved learning [78, 83] but impose substantial demands on memory, energy, and compute resources. Recent research has focused on various model compression techniques such as pruning [3, 18] and quantization [23, 34, 42, 63] to reduce memory footprint and computational costs, and make FM inference service more accessible to resource-constrained devices.

*Model pruning* [18] reduces memory footprint by removing ineffectual model parameters, such as individual weights (unstructured) or blocks of weights (structured), and storing sparse tensors in a compressed format [30]. However, pruning of FMs may be infeasible due to, significant accuracy drops even at low pruning ratios [37, 79] and potential demand for compute and memory-intensive fine-tuning to regain accuracy. *Model quantization*, on the other hand, reduces the size of a target model by representing weights and/or activations at low precision [34, 58, 59]. Recent works on quantization [13, 23] have identified that quantizing LLMs is considerably more challenging than quantizing traditional DNNs [41, 71] due to the emergence of large magnitude features known as *outliers* [81]. These outliers significantly impact model accuracy.

**Table 1: Comparison of MicroScopiQ with prior outlier-aware co-design techniques in group A [53, 81] and B [23].**

Categories	Methods		
	Group A	Group B	MicroScopiQ
Accuracy	✔ High	✘ Low	✔ High
Effective bit-width	✘ High (18.17b)	✔ Low (2b)	✔ Low (2.36b)
Flexibility	✘ No	✘ No	✔ Yes
Aligned memory	✘ Unaligned	✔ Aligned	✔ Aligned
PE design	✘ Complex	✘ Complex	✔ Simple
HW overhead	✘ High	⚠ Moderate	✔ Low

To address the issue of outliers in FMs, recent algorithm/ architecture co-design techniques [23, 42, 63] have proposed different types of outlier-aware quantization. These techniques can be broadly categorized based on their outlier handling approach: **A** Maintaining outliers at higher precision compared to the inliers, or **B** Quantizing outliers at the same precision as inliers while using different data formats or scaling factors for outliers.

Techniques in group **A**, such as OWQ [39], SpQR [14] (algorithm) and GOBO [81], OLAccel [53], SDQ [31] (architecture co-design) exhibit low accuracy degradation. This is because they typically store outliers at high precision separated from lower precision inliers. However, these techniques result in, (a) low compression factor with high *effective bit-width* (EBW<sup>1</sup>) and (b) inefficient hardware and unaligned memory access.

On the other hand, techniques in group **B**, such as AWQ [42] (algorithm) and OliVe [23] (architecture co-design) quantize outliers at the same precision as inliers following different strategies. AWQ tries to identify a separate outlier-specific scale factor via channel-wise scaling. OliVe uses the "flint" data format [24] for inliers and "abfloat" [23] for outliers, both at 4-bit precision. These techniques mitigate the unaligned memory access while providing high compression. However, they suffer from significant accuracy degradation, particularly at ultra-low bit widths. This may be attributed to the reduced representational range available to outliers at ultra low-precision. Additionally, these methods [23] rely on a specific kind of locality of presence for the outliers, that might not be true for all the FMs, as we shall demonstrate in this work (§3.1).

Based on the limitations of existing solutions discussed above, we identify that assignment of higher bit-width for outliers is essential for good accuracy while for aligned memory and hardware efficiency a consistent *bit-budget*<sup>2</sup> and data type per tensor element is desired. Here, by consistency we mean that on average each scalar should be represented by a fixed bit-width of a particular data-type. However, these demands are generally conflicting.

**Contributions.** To provide a unified solution, we investigate on a fundamental question: *Can pruning be effectively leveraged to*

<sup>1</sup>The average number of bits used to represent each quantized parameter of a model.

<sup>2</sup>number of bits per weight/activation element

complement outlier-aware quantization in achieving high accuracy while maintaining hardware efficiency?

Towards achieving this, we present a novel co-design technique for the post-training quantization (PTQ) of FMs, namely **MicroScopiQ**. Our approach effectively leverages pruning with outlier aware quantization to achieve both memory alignment and improved accuracy. To effectively perform this, for a layer we prune the least important weights based on the Hessian information, and redistribute the additional bits of the outlier weights in the pruned locations. This ensures memory alignment while allowing outlier weights to have higher precision. Additionally, to maintain low error we use the recently proposed MicroScaling (MX) FP data format [12, 60] to quantize outlier weights compared to MX-INT inlier quantization. To efficiently support outliers in a **different** format with **different** bits at **different** locations, we present an intelligent NoC architecture called, Redistribution and Coordination NoC (ReCoN). It offers minimal overhead and high throughput outlier processing and reorganization. We then present an accelerator that leverages ReCoN with a simple, homogeneous INT-PE array. Further, we extend the accelerator to be generic enough to support multiple bit-precision (2/4-bit operations). As summarized in Table 1, MicroScopiQ blends the advantages of group **A** and **B** techniques while mitigating their specific drawbacks.

Our key contributions can be summarized as follows:

- We present MicroScopiQ, a PTQ framework to efficiently integrate pruning with outlier-aware quantization (§4).
- To effectively deploy MicroScopiQ in a systolic array architecture we present a novel architecture supporting multi-precision, homogeneous PEs with a low-overhead NoC architecture (§5).
- To our best knowledge, MicroScopiQ is the first co-design technique, to push the limits of PTQ compression for **both** LLMs and VLMs with an EBW of **~2.36-bits** for weights; achieving SoTA quantized model accuracy across different weight/weight-activation quantization settings. Moreover, it demonstrates up to **3× improvement in performance-per-unit-area** ( $TOPS/mm^2$ ) and up to **35% energy reduction** compared to existing architectures (§6).

## 2 Background

### 2.1 Model Quantization

A typical quantization [41, 58] process involves two steps: establishing the quantization parameters, given the quantization data format ( $\tau$ ) and bit-width ( $b$ ), and mapping the high-precision tensor to the quantized representation. For a typical symmetric quantization [85] (zero-point is 0) of a tensor  $X$ , the *scale factor* ( $s$ ) is given by,

$$s = \frac{\max(X)}{\max_{\tau}^b} \quad (1)$$

$\max_{\tau}^b$  is the maximum representable value of a data format [58]. For  $b$ -bit INT quantization,  $\max_{INT}^b = 2^{b-1} - 1$ . After determining the quantization parameters, the quantized tensor is given by [58],

$$Q(X, s, b) = \text{clip}\left(\left\lfloor \frac{X}{s} \right\rfloor, \min_{\tau}^b, \max_{\tau}^b\right) \quad (2)$$

In model quantization, the quantization parameters can be shared at different granularity for different accuracy-overhead trade-offs. In increasing order of overheads, we have **per-tensor** quantization, wherein the scale factor is shared among all tensor elements. In **per-channel** quantization, the scale factor is shared per row/column of

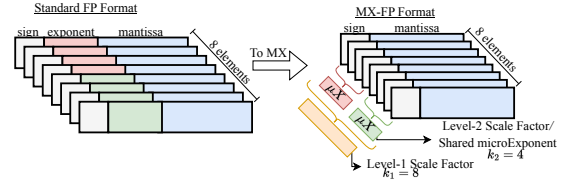


**Figure 1: Depiction of MX-FP data format with level-1 scale factor and level-2 microExponent ( $\mu X$ ), with  $k_1$  and  $k_2$  the group sizes over which these two factors are shared.**

a tensor. Finally, in **group** quantization, the parameters are shared at a finer granularity between groups of  $k$  (64, 128 etc.) elements in a row or column. These groups are formed by dividing channels into multiple non-overlapping contiguous blocks. *In this paper, we adopt MX-INT and MX-FP quantization for inliers and outliers, respectively.*

### 2.2 Microscaling Data Format

The MX data format proposed by prior works [12, 60], is standardized by the Open Compute Project [55] with support from Microsoft, Intel, NVIDIA and others. As shown in Figure 1, MX is a variant of block data representation (BDR) [12] that defines a format to represent a group of values collectively using shared scale factors. It leverages multi-level, power-of-two scaling, at fine- (level-1,  $k_1$ ) and ultra-fine (level-2,  $k_2$ ) granularity [11, 16]. The MX data format is characterized by four components: i) scale factors (level-1, 2), ii) data type ( $\tau$ ), iii) bit-width ( $b$ ) and iv) group sizes ( $k_1, k_2$ ). In this paper we denote an MX-FP format as  $MX-FP-b_{k_1, k_2}$ . In this work, we adopt the version of the MX-FP data format proposed in [60], employing multi-level scaling. The level-1 scale factor for MX-FP is computed following Equation 1. Conversely, for level-2 scale factor, we identify that MX-FP leverages the sharing of exponent field of FP values [75] (referred as  $\mu X$  in Figure 1). We show in §4.2 that by taking advantage of this insight i.e., the concept of shared  $\mu X$ , we are able to represent FP-outliers in INT format, thereby, enabling the design of simple, homogeneous INT-based PEs. For inliers, we employ  $MX-INT-b_{k_1}$  with a single level of scale factor following [55]. This is because, INT format does not possess an exponent field, thereby, a level-2 scale factor similar to MX-FP is not applicable. For simplified understanding,  $MX-INT-b_{k_1}$  inlier quantization can be viewed as analogous to INT group quantization utilizing an E8M0 scale factor.

## 3 Motivation

### 3.1 Limitations of existing techniques

In Table 1, we compare candidate proposals from group **A**: GOBO [81] and group **B**: OliVe [23] across various metrics. GOBO is able to achieve high accuracy by retaining outliers at full-precision. It stores outliers separately from low-precision inliers by using sparse representations with the associated outlier indices (see Figure 3(b)). By retaining outliers at full-precision, GOBO results in high EBW. Moreover, the compressed sparse storage and multiple precisions results in unaligned and random memory accesses [23], significantly impacting inference latency. Furthermore, GOBO’s outlier handling is hardware inefficient, requiring complex PEs. Similarly, a recent work [31] proposed to decompose a vector of weights into two separate inlier and outlier vectors each quantized in different precisions with outliers at a higher precision.

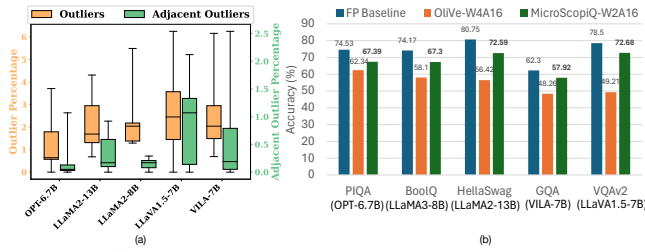


**Figure 2: ((a) Layer-wise distribution of outliers and adjacent outliers as a percentage of total number of weights, (b) Quantization accuracy comparison between OliVe-W4A16 and MicroScopiQ-W2A16 on various benchmarks.**

OliVe [23] proposes a scheme to ensure aligned memory access by quantizing inliers and outliers at the same precision (low EBW), but using different data formats. To enable differentiation between the inlier and outlier formats, it prunes the value adjacent to the outlier for use as an identifier (see Figure 3(c)). However, OliVe results in significant accuracy degradation, especially at low precision (see Figure 2(b)), due to: 1) sacrificing a number encoding from inliers for exclusive use as an identifier, reducing the number of representable values in the quantized range, and 2) the rigid assumption of outlier locality—that outliers are never adjacent to each other and only inliers are almost always adjacent to outliers (see §3.2), leading to unintended outlier pruning. Furthermore, OliVe requires a fairly complex PE design incurring significant encoding/decoding overheads to convert the different formats into a unified processing format (exponent-integer pair). We show that despite quantizing outliers at higher-precision and in a different format, we ensure aligned memory access, simple PE design and minimal hardware overhead.

### 3.2 Adjacent Outliers Matter

Similar to prior works [23, 53], we leverage the  $3\sigma$  rule [56] to categorize weights as outliers. We visually demonstrate the distribution of outliers and adjacent outliers<sup>3</sup> as a percentage of the total number of weights in a layer across different FMs in Figure 2(a). As the orange box-plot shows, outliers depict a maximum percentage of  $\sim 5.1\%$ . Outliers are prevalent in FMs, and preserving their values is crucial for maintaining quantized model accuracy. **Importantly**, from the green box-plots, we observe that modern FMs on average possess  $> 0.5\%$  adjacent outliers per layer, with some FM layers showing peaks of  $> 2\%$ . This is in stark contrast to the models evaluated by OliVe, such as BERT [15] and OPT [84] which have  $< 0.04\%$  adjacent outliers (two orders of magnitude lower than FMs like LLaMA3 and LLaVA). This indicates that while pruning values adjacent to outliers could have been ideal for models like BERT [15], it is sub-optimal for most modern FMs as it removes crucial outlier values, leading to higher accuracy degradation. This is evident from Figure 2(b) where OliVe has significant accuracy degradation at 4-bit quantization due to its assumption on outlier locality. *Unlike OliVe, MicroScopiQ does not naively prune adjacent values; instead it leverages the Hessian information [19] to identify the least important values to prune, ensuring outlier preservation. This directly translates to high quantized model accuracy and MicroScopiQ at 2-bit consistently outperforms OliVe across different FMs.*

<sup>3</sup>We define adjacent outliers as two contiguous outliers along the dot-product dimension (see row 2 of the LLM weight matrix in Figure 3).

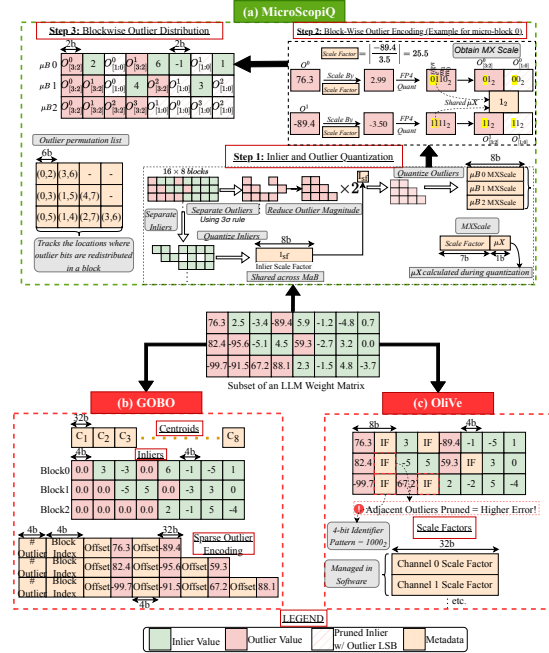


**Figure 3: (a) Overview of the proposed MicroScopiQ quantization framework depicting methodology of inlier and outlier quantization and redistribution of outlier bits for a sample LLM weight matrix. Comparison against prior quantization frameworks (b) GOBO, and (c) OliVe.**

### 3.3 Outlier Precision and Data Format

The ability of group  $\mathbb{A}$  techniques like GOBO [81] to achieve high quantized model accuracy even at extreme quantization levels of inliers ( $< 4$ -bits) is due to retaining outliers at higher precision. This is particularly crucial at ultra-low bit width quantization because, if inliers and outliers are to be quantized to the same precision, there will be higher outlier quantization error due to the reduced representational range. We demonstrate this effect on the MicroScopiQ quantized FM accuracy in Table 6 wherein the quantized FM has poor performance when inliers and outliers are at 2-bits compared to outliers at 4-bits. Furthermore, evidence from recent work [76] demonstrates that FP-based formats for LLMs results in superior quantization performance compared to INTs. To validate this, we compare MX-INT v/s MX-FP inlier and outlier quantization in Table 6. Evidently using MX-FP instead of MX-INT for outliers results in better performance. This is due to the higher dynamic range of FPs, which is particularly beneficial at extreme quantization levels. *In this work, we quantize outliers at a higher precision (2 $\times$ ) compared to inliers, using MX-FP for outliers and MX-INT for inliers.*

## 4 MicroScopiQ Quantization Methodology

We present an overview of MicroScopiQ quantization in Figure 3(a) and detail it in Algorithm 1. MicroScopiQ supports various group size granularities and any inlier and outlier (2 $\times$  inliers) data precision. For simplicity, we explain with inlier and outlier precision of 2/4- and 4/8-bit and group sizes of 128 for inliers and 8 for outliers.

### 4.1 Preliminaries

The MicroScopiQ quantization framework models the layer-wise post-training quantization of FMs by partitioning each layer into

multiple rows and quantizing each row at a time. Concretely, for a given input calibration dataset  $\mathbb{X}$ , at layer  $l$  the objective is to find a quantized set of weights  $\mathbb{Q} \in \mathcal{R}^{d_{row} \times d_{col}}$  that minimizes the sum of squared errors over all rows of the layer compared to the full-precision weights  $\mathbb{W} \in \mathcal{R}^{d_{row} \times d_{col}}$ . This can be formulated as,

$$\operatorname{argmin}_{\mathbb{Q}} \sum_{i=1}^{d_{row}} \|\mathbb{W}_{i,:} \mathbb{X} - \mathbb{Q}_{i,:} \mathbb{X}\|_2^2 \quad (3)$$

We evaluate the second order derivative of Equation 3, namely the Hessian [26, 38] through Taylor series expansion [26]. Note, the Hessian is the same for all rows depending only on input data and is given as,  $\mathbb{H} = 2\mathbb{X}\mathbb{X}^T$ . Its inverse is,  $\mathbb{H}^{-1} = (2\mathbb{X}\mathbb{X}^T + \lambda\mathbb{I})^{-1}$ . We leverage the Hessian information to identify weights with small ‘‘salencies’’ for pruning (L17 in Algo. 1). The number of inliers to prune is determined by the number of outliers, as detailed later.

To improve quantization performance, we take inspiration from [19] and adjust the weights of unquantized rows to minimize the net error while quantizing a particular row of weights. The associated equation (L31 of Algo. 1) for weight update using the Hessian is derived by solving the Lagrangian of Equation 3. However, updating all remaining rows each time a row is quantized incurs significant compute-overhead, making this intractable for billion-scale FMs. Therefore, as pointed out in [19], we partition the rows into non-overlapping contiguous row-blocks (rB) of size 128 rows and localize the updates of unquantized rows within each rB. We only update the rows outside a rB (L36 in Algo. 1) once all the elements of the current block are quantized. This minimizes the number of individual updates by grouping updates together per rB and producing an order of magnitude speedup.

## 4.2 Inlier and Outlier Weight Quantization

In step 1, each row to be quantized is first divided into multiple non overlapping contiguous **macro-blocks (MaBs)** of size  $B_M = 128$ . All inliers are quantized within a MaB and share the scale factor. Each MaB is then subdivided into multiple non-overlapping contiguous **micro-blocks ( $\mu$ Bs)** of size  $B_\mu = 8$  with sixteen  $\mu$ Bs forming a MaB. The outliers present in each  $\mu$ B shares same scale(s). As depicted in Figure 3(a), step 1, the quantization process begins by first identifying inliers and outliers in each MaB by using the  $3\sigma$  rule. A shared 8-bit power-of-two scale factor ( $2^{I_{sf}}$ ), following Equation 1 is calculated for all inliers in a MaB and the inliers are quantized to 2-bit or 4-bit, resulting in MX-INT-(2/4)<sub>128</sub> quantization. Interestingly, **we observe that the inlier scale factor in each MaB is always a negative power of two** for all FMs under consideration. We leverage this observation to **reduce outlier magnitude**, by multiplying all outlier values in a MaB with the inlier scale factor ( $2^{I_{sf}}$ ) (can also be perceived as division by  $2^{-I_{sf}}$ , for conformity with Equation 2). This pre-processing helps make outlier quantization easier, by pre-reducing its dynamic range.

Unlike inliers, outliers are quantized per  $\mu$ B, to reduce quantization error due to shared scaling over a larger group size (see §6). After identifying outliers present in a  $\mu$ B, we compute a shared 8-bit MXScale that is calculated by concatenating the level-1 power-of-two scale factor ( $2^{O_{sf}^1}$ ) and level-2 microExponent ( $\mu X$ ). The level-1 scale factor is calculated by following Equation 1 to obtain 7 or 5-bit MSBs of MXScale depending on size of  $\mu X$  being 1 or 3-bit of the LSBs—corresponds to exponent size of the FP format (depicted

## Algorithm 1: MicroScopiQ Quantization Framework

---

**Input** :  $\mathbb{W} \in \mathcal{R}^{d_{row} \times d_{col}}$ , calibration data  $\mathbb{X}$ ,  $\mathbb{H}^{-1} = (2\mathbb{X}\mathbb{X}^T + \lambda\mathbb{I})^{-1}$ , row block (rB), macro-block (MaB)  $B_M$ , and micro-block ( $\mu$ B)  $B_\mu$

**Output**: Quantized weight  $\mathbb{Q} \in \mathcal{R}^{d_{row} \times d_{col}}$ , perm (Permutation list)

```

1 # Iterate over row blocks
2 for  $i = 0, rB, 2rB, \dots, d_{col} - rB$  do
3   for  $j = i, i+1, \dots, i+rB-1$  do
4     # Step 1.0: Divide each row into non-overlapping Macro-Blocks
5     for  $\mathbb{W}_{j, MaB} \in \mathbb{W}_{j,:}$  do
6       # Step 1.1: Separate inlier and outlier in each Macro-Block
7        $\mathbb{W}_{j, MaB}^{in}, \mathbb{W}_{j, MaB}^{out} = \text{sep\_in\_out}(\mathbb{W}_{j, MaB})$ 
8       # Step 1.2: Quantize Inliers to lower precision
9        $\mathbb{Q}_{j, MaB}^{in}, I_{sf} = \text{InlierQuantization}(\mathbb{W}_{j, MaB}^{in})$ 
10      for  $\mathbb{W}_{j, \mu B} \in \mathbb{W}_{j, MaB}^{out}$  do
11        # Step 2.0: Count Number of Outliers in a Micro-Block
12         $n = \min(B_\mu/2, \text{NumOutliers}(\mathbb{W}_{j, \mu B}^{out}))$ 
13        # Step 2.1: Initialize Inlier Index List
14         $M \leftarrow \emptyset$ 
15        # Step 2.2: Identify  $n$  least Important Inlier Position
16        for  $n$  iterations do
17           $p = \operatorname{argmin}_{p \in \mathbb{W}_{j, \mu B}^{in}} w_p^2 / \lceil \mathbb{H}^{-1} \rceil_{pp}$ 
18          # Step 2.3: Prune least important Inliers
19           $w_p \leftarrow 0$ 
20          # Step 2.4: Update  $M$  with the location of  $w_p$ 
21           $M \leftarrow M + \{p\}$ 
22        end
23        # Step 2.5: Quantize Outliers to higher precision
24         $\mathbb{Q}_{j, \mu B}^{out}, O_{sf} = \text{OutlierQuant}(\mathbb{W}_{j, \mu B}^{out}, I_{sf})$ 
25        # Step 3.0: Distribute LSB Outlier Bits to Sparse Inlier Indices
26        perm  $\leftarrow \text{DistributeOutlierBits}(\mathbb{Q}_{j, \mu B}^{out}, M)$ 
27      end
28       $\mathbb{Q}_{j, MaB} = \mathbb{Q}_{j, MaB}^{in} + \mathbb{Q}_{j, MaB}^{out}$ 
29    end
30    # Step 3.1: Quantization Error
31     $\mathbb{E}_{(j-i),:} = (\mathbb{W}_{j,:} - \mathbb{Q}_{j,:}) / \lceil \mathbb{H}^{-1} \rceil_{jj}$ 
32    # Step 3.2: Update weights in rB to compensate quantization error
33     $\mathbb{W}_{j:(i+rB),:} = \mathbb{W}_{j:(i+rB),:} - \mathbb{E}_{(j-i),:} \cdot \mathbb{H}_{j:(i+rB),j}^{-1}$ 
34  end
35  # Step 3.3: Update remaining weights after a row block is quantized
36   $\mathbb{W}_{(i+rB),:} = \mathbb{W}_{(i+rB),:} - \mathbb{E} \cdot \mathbb{H}_{(i+rB),:(i+rB)}^{-1}$ 
37 end
```

---

in step 2 in Figure 3(a)). The outliers in a  $\mu$ B are scaled by ( $2^{O_{sf}^1}$ ), following Equation 2 and then quantized to either  $e1m2/e3m4$  FP-format for  $b = 4$  or 8-bit, respectively. Post quantization of outliers, the level-two scale factor or the  $\mu X$  is obtained by extracting the common exponent among all outliers in a  $\mu$ B. This process results in a MX-FP- $b_{8,8}$  outlier quantization. The final outlier scale factor is  $2^{O_{sf}}$  where,  $O_{sf}$  is expressed as  $O_{sf} = O_{sf}^1 + \mu X - I_{sf}$ . The term  $I_{sf}$  in the final outlier scale factor accounts for multiplication by  $2^{I_{sf}}$  (or division by the inverse) during outlier pre-processing.

## 4.3 Outlier Value Encoding through N:M Structured Pruning

To formalize step 2, let us assume  $n$  outliers are present in a  $\mu$ B quantized to MX-FP-4<sub>8,8</sub>. After sharing 1-bit  $\mu X$  across the  $n$  outliers, each outlier has 1 sign (s) and 2 mantissa bits ( $m_1 m_0$ ). The inliers are 2-bit 2’s complement MX-INT and has 1-bit sign and 1-bit magnitude. Since the outlier bits have two mantissa bits with one sign, to ensure symmetric outlier distribution, we duplicate their sign bit and assign each sign to a mantissa creating and partitioning into two halves Upper, Lower of size 2-bit each mimicking inlier MX-INT structure i.e.,  $\{sm_1, sm_0\}$  (see Figure 3(a), step 2). While we demonstrate this for a specific example, the process can be generalized to other inlier and outlier formats bit-widths, wherein

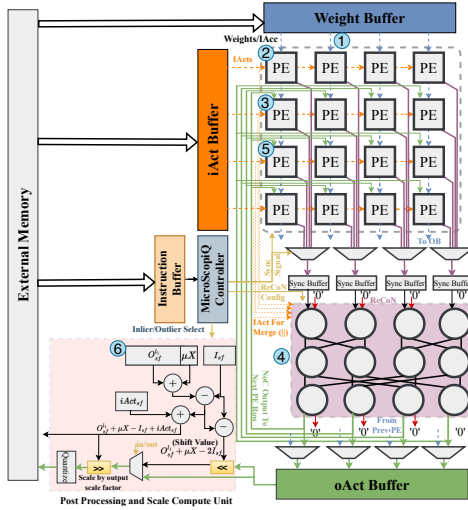


**Figure 4: Integration of MicroScopiQ into a WS systolic array.** the remaining outlier bits need to be reorganized into Upper and Lower distributable halves each of size  $bb$  (per element bit-budget), with  $bb$  representing the operational bit-width of each PE.

In step 3, to ensure a fixed  $bb$  and data-type of a layer for aligned memory access and simple PE design, we distribute the outlier LSBs (Lower half) to the least important inlier locations that are pruned within a  $\mu B$ . For  $n$  outliers in a  $\mu B$  we identify  $n$  least important inlier locations to prune via the Hessian information (see Algorithm 1), forming a  $(B_\mu - n) : B_\mu$  structured pruning pattern [30, 70] i.e.,  $(B_\mu - n)$  non-zero values exist per  $\mu B$  after pruning. To keep track of the corresponding halves of each of the outliers in a  $\mu B$ , we maintain a per- $\mu B$  permutation list (Note: if there are no outliers in a  $\mu B$ , a permutation list is not stored). The permutation list for each  $\mu B$  that has outliers is made up of  $\frac{B_\mu}{2}$  elements (maximum number of outliers supported per  $\mu B$ ) with each element storing the locations of the Upper and Lower halves of outliers in a 6-bit format  $\{\text{Upper}_{loc}, \text{Lower}_{loc}\}$  (see Figure 3(a) step 3). Note that, in case of outlier count  $> \frac{B_\mu}{2}$ , the  $mB$  size should be chosen to be higher to prevent pruning of outliers and causing higher accuracy degradation. While such a situation does not arise in any of the models that we evaluate with  $B_\mu = 8$ , this feature only serves as a demonstration of the flexibility of MicroScopiQ for future models.

#### 4.4 Effective Bit Width (EBW) Calculation

Following [19, 85] we report the EBW as the average number of bits required for storing each element including the metadata. The EBW of MicroScopiQ quantized FM varies dynamically across models and is dependent on the outlier percentage and choice of  $\mu B$  size. For INT- $2B_M$  inlier and MX-FP- $4B_\mu, B_\mu$  outlier quantization, if there are no outliers in a  $\mu B$  the EBW of that  $\mu B$  is  $EBW_I = 2$ , i.e.,  $bb$ , whereas if there are outliers present in a  $mB$  the EBW is  $EBW_O = (\text{perm}^{bits} + 2B_\mu + O_{sf}^{bits})/B_\mu$ , which translates to 6-bits for  $B_\mu=8$ , MXScale of 8-bits and permutation list size of 24-bits (see §4.3). Since the inlier scale factor is shared across a larger group size  $B_M$ , its contribution to the EBW is negligible and hence ignored. As a rule of thumb, if there are no outlier present in a  $\mu B$  the EBW of that  $\mu B$  is equal  $bb$  else the EBW includes the contribution of all outlier-specific metadata. The presence or absence of outlier metadata is delineated

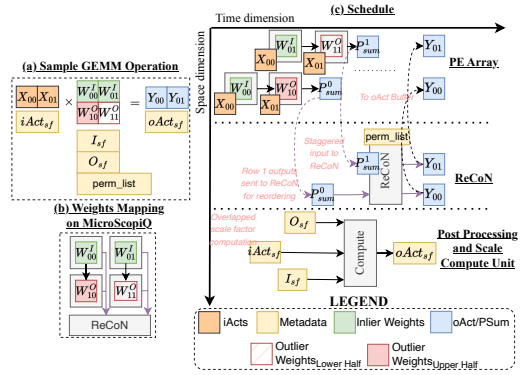


**Figure 5: Example scheduling of a GEMM operation on a  $2 \times 2$  MicroScopiQ accelerator.**

by a 1-bit identifier per  $\mu B$ , wherein a 0 indicates no outlier metadata and vice versa. This identifier contributes negligible overhead to the EBW (0.05-0.09 bits) similar to the inlier scale factor and is hence ignored in the EBW calculation. For a FM with  $l$  layers and each layer having  $m$   $\mu B$ s and  $x\%$  of these  $\mu B$ s consist of outliers, the EBW of the FM is,

$$EBW_{FM} = \frac{\sum_{i=1}^l (x \cdot m \cdot EBW_O + (100 - x) \cdot m \cdot EBW_I)/m}{l} \quad (4)$$

## 5 MicroScopiQ Accelerator

### 5.1 Architecture Overview

In Figure 4, we depict the MicroScopiQ accelerator architecture, integrated into a standard weight stationary systolic array. The accelerator is optimized for throughput and all compute units (PE array, ReCoN etc.) are internally **pipelined** with interleaved pipeline stages. Through the numbered steps in Figure 4, we explain the computational flow of the MicroScopiQ accelerator. And in Figure 5(a-c), we demonstrate the mapping and schedule for a sample  $2 \times 2$  GEMM operation with inlier and outlier weights, following the same computation flow.

Assume a quantized FM with outliers distributed within a  $\mu B$  and corresponding metadata calculated offline.

① One  $\mu B$  or multiple  $\mu B$ s of weights are mapped to each PE row as typically  $B_\mu \leq \#$  of columns in PE array [33]. Each PE in a row either receives a weight at high-precision (e.g. 4-bit) or multiple packed weights at low-precision (e.g. two 2-bits).

② PE row 0 receives quantized input activation (iAct) from left and input accumulation (iAcc) from top. The PEs in row 0 perform multiplication of the stationary weights with the iActs, regardless of outlier/inlier weights. During accumulation, assuming the  $\mu B$ s mapped to PE row 0 do not contain outliers (see Figure 5(c)), the PEs accumulate the computed multiplication result with iAcc and direct the partial sums to PE row 1.

③ PE row 1 receives partial sums from the top and similarly performs INT multiplication between weights and iAct. As shown in the scheduling figure, in parallel, the output scale factors can be calculated (§5.5). ④ The mapped  $\mu B$ s to PE row 1 have outliers, the controller directs all PE outputs to ReCoN. PE row 1 offloads the accumulation to ReCoN (shown by dotted lines in Figure 5(c)). This is needed because the outlier will have its two halves distributed in different locations and mapped to different PEs. While the PEs in row 0 with inlier weights can accumulate the partial sum output,

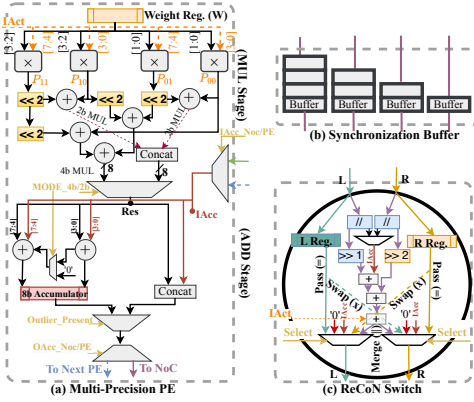


**Figure 6: Microarchitecture of (a) Multi-precision PE, (b) Synchronization buffer and (c) ReCoN switch.**

the PEs in row 1 with the Upper and Lower outlier halves cannot compute the outlier partial sum output. After receiving outputs from row 1, ReCoN reorders and calculates the FP-outlier partial sum.

⑤ The controller signals PE row 2 to expect input partial sums from ReCoN and not from the previous row. If PE row 1 is the last row as in Figure 5(c), the oActs are directed to the oAct buffer.

⑥ oActs are post-processed (scaled and quantized). The post-processing of oActs does not require all the oActs to be computed. The post processing operations can be conducted as and when the oActs are generated and overlapped with the rest of the computation so as to hide computation and memory access latency overhead.

## 5.2 On-chip Storage and Control

**Weight/Activation Organization.** The iActs are stored in the iAct buffer as 8-bit INTs. Lower-precision iActs (<8-bit) are supported through sign-extension. The same process is followed for oActs. The weight buffer stores weights at 4-bit granularity. At lower precision (2-bits), each buffer location simultaneously stores two 2-bit weights. The **MODE** signal from the controller identifies the interpretation of bit format of weights in the weight buffer i.e., one 4-bit weight or two 2-bit weights.

**Instruction Buffer (IB).** It stores all the metadata required for inference of MicroScopiQ quantized FMs. Particularly, the IB stores the outlier distribution permutation list i.e., configurations for ReCoN and scale factors.

**MicroScopiQ Controller.** The controller generates appropriate control and signals to all units. It is functionally very similar to standard systolic array controllers [66], however, with added functionality to support specific features of ReCoN (arbitration of simultaneous access by multiple rows), multi-precision PEs, post-processing unit. Furthermore, unlike traditional controllers, the MicroScopiQ controller exerts fine-grained control using handshaking signals on the streaming of iActs, iAccs into the PE array to account for the increased pipeline depth through ReCoN for rows with outliers.

## 5.3 Multi-Precision PE Array

**Multi-Precision.** We depict the multi-precision MicroScopiQ PE in Figure 6(a). Existing multi-precision accelerators [23, 24, 66] typically follow a bottom-up approach, employing low-precision PEs and grouping neighboring PEs to support higher precision. This

sacrifices throughput for multi-precision support, as multiple PE columns are required to perform a single MAC operation. This reduces parallelism and increases latency. We adopt a different strategy via the **MODE** signal for multi-precision support by mapping multiple weights that share the same rightbound iAct to the same PE at lower precision (2-bits) or a single weight at higher precision (4-bits). The two 2-bit weights mapped to the same PE in MicroScopiQ are the weights that would have been mapped to different columns within the same row in existing multi-precision accelerators. At high-precision operation we utilize available parallelism from the PE array while at lower-precision we increase throughput by the parallel evaluation of multiple partial sums.

**Multiplication Stage.** Inspired by [45, 74] we present a multiplier-tree architecture for multi-precision INT multiplication. The weights and iAct are partitioned across the four 4-bit  $\times$  2-bit multipliers to calculate partial sums ( $P_{00}, P_{01}, P_{10}, P_{11}$ ) as described in Figure 6(a). Based on the **MODE** signal the partial sums above are combined using a combination of adders and shifters to provide the result (**Res**) of different bit-precision weights with iAct as follows,

$$\text{Res} = \begin{cases} \{(P_{11} \ll 2 + P_{10}), (P_{01} \ll 2 + P_{00})\}, \text{MODE}_{2b} \\ (P_{11} \ll 4 + P_{00}) + (P_{01} \ll 2 + P_{10} \ll 2), \text{MODE}_{4b} \end{cases} \quad (5)$$

**Accumulation Stage.** It receives the MUL-stage output (**Res**) and also iAcc from either ReCoN or the previous PE row. The controller signals the ADD stage via **Outlier\_Present** to modify accumulation behavior based on whether inlier/outlier weights are present in the PE. If the **Res** corresponds to a multiplication of inlier weight with iAct, then the corresponding **Res** is added with iAcc using two adders with a multiplexer that enables multi-precision by propagating the carry from one adder to other. In low precision **MODE**, the two adders work independently to calculate partial sums in parallel. For high precision **MODE**, both adders work together to produce a single accumulation result with carry propagation through the multiplexer. On the other hand, if **Res** corresponds to multiplication of either of the outlier halves with iAct, the actual outlier accumulation is offloaded to ReCoN by concatenating **Res** and iAcc<sup>4</sup>. This is done to prevent incorrect outlier partial sum calculation. The controller directs partial sum outputs to ReCoN or next PE row based on presence of outliers, via the **OAcc\_NoC/PE** signal.

## 5.4 Redistribution and Coordination NoC

The Redistribution and Coordination NoC (ReCoN) is a multistage butterfly NoC in the MicroScopiQ accelerator **time-multiplexed** and shared across PE rows (see §6.6). This is a more **cost effective** way of handling outliers compared to OliVe and GOBO [23, 81] that handle outliers within the PE. Since **PEs are large in number** OliVe, GOBO will incur larger costs compared to MicroScopiQ.

**ReCoN topology.** ReCoN is composed of  $n(\log_2(n) + 1)$  {2-input, 2-output} ReCoN switches, in a multistage butterfly NoC topology [36]. The input and output stages of ReCoN also employ {2-input, 2-output} switches, with a dedicated switch for each column receiving (transmitting) partial sums into (from) one of the two input (output) ports. The other port of the input and output stages of each switch is tied to 0. Each ReCoN stage also receives the same iActs used by the PEs to compute the partials sums. As we shall show later, this is done to facilitate FP-outlier’s hidden-bit processing.

<sup>4</sup>the concatenated output is notated as  $O_{\text{Upper,Res}}$  or  $O_{\text{Lower,Res}}$ .

**ReCoN Input Interface.** ReCoN is shared and time-multiplexed across all PE rows, and at a particular instant many rows might require access to it. At the inputs, the column-wise arbiters guided by control signals from the controller, coordinate and resolve contention between different PE rows and ensure a fair scheduling (Note for simplicity in Figure 4, we conceptually depict this operation as a N-input multiplexer). Due to the skewed data flow of systolic array computations [33, 59], partial sums from different columns of the same row do not arrive at the ReCoN input at the same cycle. A synchronization buffer (Figure 6(c)) is positioned between ReCoN and column-wise multiplexers which propagates the partial sums through sets of buffers of different lengths (column producing the partial sum fastest has the most buffers), synchronizing the arrival of inputs from different columns. The synchronization buffer sends an ACK signal to the PE row whose values have been accepted so that it can progress in its computation and the other simultaneously contesting rows will be on hold and acknowledged in the next cycle. When there are N simultaneously contesting rows, the row that is acknowledged the last adds an N-1 cycle latency to its processing. As we show in Figure 10(b), Figure 13(a) the num. of conflicts in accessing ReCoN are minimal and if latency is a critical factor multiple ReCoN units can be used to minimize conflicts.

**ReCoN switch.** It is a {2-input, 2-output} switch (Figure 6(c)) that performs three major operations based on a 3-bit configuration:

- Pass (=): Passes the input from left (right) port to left (right) output port.

- Swap (×): Directs the input from the left (right) input to the right (left) output, with the opposite output port receiving the right (left) port input, 0 or iAcc (see§5.6).

- Merge (||): This function is triggered when a switch receives  $O_{Upper,Res}$  and  $O_{Lower,Res}$  at its left and right ports, respectively. The switch separates the Res from iAcc (denoted as // in Figure 4) from both inputs and selects the Upper result’s iAcc, since it is the correct iAcc for accumulation ( $O_{Lower,Res}$  iAcc is selected during Swap). The Upper and Lower halves of outlier weight’s magnitude bits are actually mantissa bits ( $< 1$ ) of MX-FP which the PE treat as INTs. Therefore the Res of  $O_{Upper,Res}$  and  $O_{Lower,Res}$  are shifted  $1\times$  and  $2\times$  respectively (not shown in figure, but internally handles multi-precision MODE) to account for the decimal position of mantissa in the MX-FP format. The shifted Res are then accumulated with the corresponding iAcc. FP-formats also have a hidden-bit (1.0) [59, 75]; to account for the contribution of the hidden bit to the outlier partial sum we also add iAct to the accumulation above.

**ReCoN Output Interface.** The reordered partial sums are then routed to the subsequent row in the PE array or if the input is from the last PE row, to the oAct buffer. Since ReCoN is pipelined internally and with the rest of the PE array, reordered and processed partial sums are produced every cycle once the pipeline depth (=number of ReCoN stages) is filled.

## 5.5 Post Processing and Output Scale Factor Computation

The shared output scale factor for  $B_M=128$  is calculated as  $oAct_{sf} = O_{sf} + iAct_{sf}$  (See expansion of  $O_{sf}$  in §4.2.). The calculation of  $oAct_{sf}$  (with simple adders and subtractors) is independent of the processing done in the PE array. Therefore, we overlap the computation of  $oAct_{sf}$  with the processing of oActs to efficiently hide

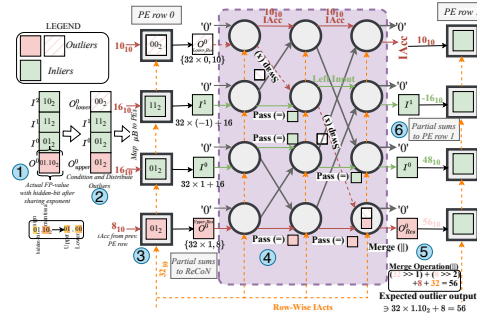


**Figure 7: End-to-end example illustrating the working of MicroScopiQ with a  $4 \times 4$  PE array (only two rows shown).**

the computation latency similar to prior works [11, 59]. Since we maintain different scales for inliers and outliers (see §4.2), and the oAct scale factor is calculated based on the outlier scale factor ( $O_{sf}$ ) (we found this to result in least quantization error of oActs), the oActs which are generated through computation with only inlier weights (identified through the in/out control signal) are shifted by the shift value depicted in the “Post Processing and Scale Compute Unit” in Figure 4 to ensure conformity with the final scale factor. Finally, the oActs are scaled with the computed output scale factor through a simple right shift (since it is a power-of-two scale factor, division can be implemented through right shift operation) and quantized to  $MX-INT-(4/8)_{128}$  before being sent to external memory or routed back to the iAct buffer for computation with the next layer’s weights. Similar to prior works [59], [35] the post processing unit is also responsible for handling all non-linear operations.

## 5.6 MicroScopiQ Walkthrough Example

In this section, we discuss an end-to-end example that concretely showcases the working of MicroScopiQ. In the example shown in Figure 7, we employ a  $4 \times 4$  systolic array (2 rows shown) with PE row 0 having one outlier and three inliers in the  $\mu B$  and PE row 1 having all inlier weights. Note: Not all rows require access to ReCoN, only rows that have one or more outlier weights (row 0) in the PE require access. We assume  $\mu B=4$ , inlier and outlier quantization formats of  $MX-INT-2_{128}$  and  $MX-FP-4_{4,4}$ , respectively.

- 1 To demonstrate that outlier partial sums processed through ReCoN results in accurate FP-outlier partial sum, we first show a  $\mu B$  with one outlier and its actual FP-value after sharing of  $\mu X$ , and having a value of  $1.5_{10}$ . If there were no outlier distribution, the actual partial sum from an “outlier-specific PE” for the shown iAct=32<sub>10</sub> and iAcc=8<sub>10</sub> will be 56<sub>10</sub>. However as described in §4.3, we distribute outliers within a  $\mu B$  into Upper and Lower halves. Note: The hidden-bit is implicit and is only shown for demonstration.

- 2 The  $\mu B$  after distributing the outlier is mapped to PE row 0.
- 3 PE row 0 computes partial sum outputs for inliers in columns 1 and 2, while it outputs  $O_{Upper,Res}$  and  $O_{Lower,Res}$  for the other two columns that have outliers. The output of PE row 0 is routed through ReCoN. In ReCoN, the inliers are passed down at all stages, since they are already present in their respective columns.

- 4 The stage 1 switch at column 3, executes a swap operation and redirects the lower half outlier output towards the upper half while simultaneously sending iAcc through the other port. This iAcc corresponds to the iAcc input to column 3 PE in row 0. This is functionally correct because, the lower half of outlier is distributed

**Table 2: Quantization Results for LLMs. We report WikiText2 [49] perplexity numbers (lower the better).**

Method	W/A	OPT [84]		Llama-2 [73]			Llama-3 [50]		Mixtral [32]	Phi-3 [1]	
		6.7B	175B	7B	13B	70B	8B	70B	8x7B	3.8B	14B
Baseline	16/16	10.86	8.34	5.47	4.83	3.31	6.13	2.85	3.84	6.33	4.31
OliVe [24]	4/16	12.20	9.09	11.52	9.34	7.23	10.29	5.65	6.19	8.57	7.81
GOBO [81]	4/16	10.97	8.71	5.79	5.03	3.45	7.11	3.53	4.22	6.64	4.78
GPTQ [19]	4/16	11.12	9.09	6.23	5.58	4.28	8.12	3.75	4.68	7.17	5.13
AWQ [42]	4/16	10.97	8.74	5.82	5.19	4.08	7.96	3.58	4.36	6.72	4.99
OmniQuant [63]	4/16	10.96	8.72	5.74	5.02	3.47	7.09	3.46	4.19	6.67	4.82
<b>MicroScopiQ (Ours)</b>	<b>4/16</b>	<b>10.91</b>	<b>8.62</b>	<b>5.65</b>	<b>5.02</b>	<b>3.42</b>	<b>6.89</b>	<b>3.25</b>	<b>4.07</b>	<b>6.61</b>	<b>4.70</b>
OliVe [23]	4/4	55.44	14.17	19.28	14.96	13.59	27.65	9.34	23.53	17.63	15.29
OmniQuant [63]	4/4	11.61	9.88	11.47	8.32	5.41	10.21	5.30	5.98	8.21	6.40
SmoothQuant [77]	4/4	19.54	17.62	20.47	15.63	17.62	29.54	19.32	37.54	18.11	15.39
Atom [85]	4/4	11.15	9.02	6.16	6.12	5.20	8.12	4.69	5.35	7.59	5.95
<b>MicroScopiQ (Ours)</b>	<b>4/4</b>	<b>10.97</b>	<b>8.95</b>	<b>6.11</b>	<b>5.57</b>	<b>4.48</b>	<b>8.12</b>	<b>4.65</b>	<b>5.03</b>	<b>6.95</b>	<b>5.41</b>
OmniQuant [63]	2/16	11.61	9.66	9.62	7.56	6.11	9.13	6.17	6.02	7.09	6.28
SDQ [31]	2/16	12.09	10.04	10.47	8.09	6.98	10.54	6.93	7.62	7.39	6.92
<b>MicroScopiQ (Ours)</b>	<b>2/16</b>	<b>11.51</b>	<b>9.42</b>	<b>8.43</b>	<b>7.06</b>	<b>6.01</b>	<b>8.97</b>	<b>5.91</b>	<b>6.02</b>	<b>7.16</b>	<b>6.03</b>
OmniQuant [63]	2/8	11.99	10.23	9.62	8.92	6.83	9.39	6.59	6.29	7.95	7.37
Atom [85]	2/8	11.95	10.13	9.23	8.54	6.33	9.13	6.35	6.14	7.46	7.29
<b>MicroScopiQ (Ours)</b>	<b>2/8</b>	<b>11.77</b>	<b>9.98</b>	<b>9.06</b>	<b>8.06</b>	<b>6.33</b>	<b>9.08</b>	<b>6.02</b>	6.17	<b>7.38</b>	<b>6.82</b>

in this column by zeroing out/pruning the inlier at that location, hence the partial sum output of that PE to the corresponding PE in the next row should only be iAcc since the original weight at that location is zero. Similarly in stage 2 of ReCoN, the switch that receives the  $O_{\text{Lower,Res}}$  from stage 1 again executes a **swap** operation. Finally in stage 3 the outlier output halves are merged together to realize  $O_{\text{Res}}^0$ , while all other switches execute pass. This merge operation results in a  $O_{\text{Res}}^0$  that matches the expected output.

5 The partial sums from ReCoN are then sent to PE row 1 which then perform MAC operations and sends it to the subsequent row since there are no outlier weights. Similarly all rows execute operations until the final partial sum is calculated.

## 6 Experimental Evaluations

### 6.1 Experimental Setup<sup>5</sup>

**Models and Datasets.** We evaluate on OPT [84], LLaMA2 [73] LLaMA3 [50], Phi-3 (SLM) [1] and Mixtral (MoE) [32] LLM model families. The VLMs evaluated are OpenFlamingo [5], VILA [43] and LLaVa [44]. We use a calibration dataset consisting of 256 random samples from the PILE dataset [20], so as to not overfit to any particular downstream domain [42]. We compare different LLMs based on perplexity (PPL ↓) on the WikiText2 [49] dataset and benchmark accuracy on 6 different tasks BoolQ [9], HellaSwag [82], PIQA [6], ARC-c [10], MMLU [27] and Winogrande [61]. Similarly, we evaluate VLMs on 5 vision-language benchmarks: COCO captioning [7], VQAv2 [22], VizWiz [25], TextVQA [67], and GQA [29].

**Algorithm Implementation.** We implement the MicroScopiQ Quantization Framework in PyTorch [54]. All FMs are quantized using a single NVIDIA H100 GPU. The complete quantization process’ runtime ranges between 30 mins.–9 hours depending on model size (3.8B to 175B), which is at par with recent SoTA techniques [19, 85].

**Algorithm Baselines.** We compare the performance of our MicroScopiQ quantization framework against existing SoTA quantization algorithms: OmniQuant [63], AWQ [42], GPTQ [19], Atom [85], SDQ [31] and co-design techniques: OliVe [23], GOBO [81].

**Accelerator Implementation.** The MicroScopiQ accelerator is implemented in Verilog RTL. We perform synthesis and PnR using

<sup>5</sup>We denote each quantization configuration by its *bb* to enhance readability and facilitate clear comparisons.

**Table 3: LLM quantization performance of MicroScopiQ augmented with OmniQuant (Omni-MicroScopiQ).**

Method	W/A	Llama-2 13B	Llama-3 70B	Phi-3 3.8B
Baseline	16/16	4.83	2.85	6.33
OmniQuant [63]	4/16	5.02	3.46	6.67
<b>Omni-MicroScopiQ</b>	<b>4/16</b>	<b>4.87</b>	<b>2.97</b>	<b>6.52</b>
OmniQuant [63]	2/16	7.56	6.17	7.09
<b>Omni-MicroScopiQ</b>	<b>2/16</b>	<b>6.58</b>	<b>5.09</b>	<b>6.89</b>
OmniQuant [63]	2/8	8.92	6.83	7.95
<b>Omni-MicroScopiQ</b>	<b>2/8</b>	<b>7.12</b>	<b>5.74</b>	<b>7.21</b>

**Table 4: Comparison of quantization performance for LLaMA2-70B on LLM benchmarks.**

Method	W/A	ARC-c [10]	HellaS. [82]	MMLU [27]	WinoG. [61]
Baseline	16/16	60.50	84.30	68.90	80.60
OliVe [23]	2/16	38.60	55.30	39.80	60.70
OmniQuant [63]	2/16	49.70	77.80	58.20	74.20
<b>MicroScopiQ</b>	<b>2/16</b>	<b>53.30</b>	<b>81.60</b>	<b>63.70</b>	<b>77.80</b>

Synopsys Design Compiler and Innovus with a TSMC 7nm technology library (See floorplan in Figure 11(b)) for area, power and latency calculations. All MicroScopiQ design variants attains a peak clock frequency of **1 GHz**. We use CACTI [52] to estimate the area and power of on-chip memories. For end-to-end performance evaluation, we design a cycle accurate simulator based on DnnWeaver [65] and BitFusion [66], following previous works [23, 59].

**Accelerator Baselines.** We compare the MicroScopiQ accelerator against OliVe [23], ANT [24], GOBO [81], OLAccel [53] and AdaptivFloat [71] across area, power and performance metrics. To demonstrate the minimal overhead of ReCoN on NoC-based **real-world** industrial and academic accelerators, we also implement and compare against baseline MTIA [17] and Eyeriss-v2 [8]. For a fair comparison, we ensure all designs attain a clock frequency of 1GHz. DeepScale [62] is employed to scale all designs to the 7nm process.

### 6.2 LLM Quantization Results

**Weight-Only Quantization.** In Table 2, we compare the WikiText2 PPL of different LLMs for W4A16 and W2A16 settings. MicroScopiQ consistently outperforms all the baselines across different models and quantization settings. At W4A16, **MicroScopiQ achieves near-lossless quantization performance**. Particularly at W2A16, the benefits of the MicroScopiQ method is evident, achieving **up to a 2.04 decrease in PPL** compared to the baselines. This is due to MicroScopiQ’s ability to quantize outliers at higher-precision and in FP-format to reduce quantization error. At W2A16, techniques like AWQ and OliVe fail ( $\geq 1e4$  PPL, not depicted in table). MicroScopiQ outperforms the SoTA training-based framework OmniQuant across all models which requires 5 – 6 $\times$  **higher runtime**. **Weight-Activation Quantization.** Similarly, we compare the quantization performance of MicroScopiQ for W4A4 and W2A8 configurations in Table 2. Due to the dynamic nature of activations, very rarely do techniques quantize outliers in activation directly [85]. Instead, most techniques [63, 77] migrate the activation outliers to weights to enable simpler activation quantization. We borrow the migration strength ( $\alpha$ ) hyper-parameter introduced in SmoothQuant [77] to migrate the difficulty of quantizing outliers in activations to weights. We find that prior techniques [63, 77] can only migrate up to 50% of activation quantization difficulty to weights, i.e.,  $\alpha = 0.5$  before beginning to introduce higher weight



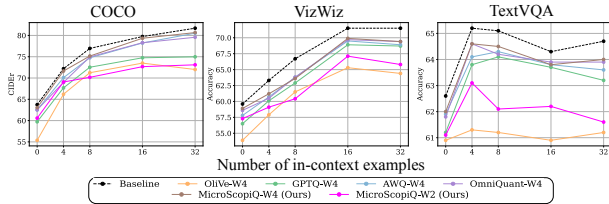


**Figure 8: Weight-only quantization for VLMs, OpenFlamingo-9B [5] on COCO and VILA-7B [43] on VizWiz and TextVQA.** quantization error. MicroScopiQ’s robustness to higher presence of outliers in weights by effectively quantizing outliers at higher precision and identifying least important weights to prune, allows  $\alpha$  as high as 0.7 i.e., migrating most of the activation outliers to weights. This enables simpler activation quantization with  $\text{MX-INT}-(4/8)_{128}$  and absolving the need to handle outliers in activations. With  $\alpha = 0.7$  for MicroScopiQ,  $\alpha = 0.5$  for SmoothQuant and learned migration strength for OmniQuant in Table 2, MicroScopiQ **outperforms all baselines with up to 7.4× lower PPL** across quantization settings. Furthermore, MicroScopiQ outperforms a recent work Atom [85] that performs activation quantization with up to a 0.33 lower PPL.

**Benchmark Accuracy.** In Figure 2(b), we compare the zero-shot task accuracy of W2A16 MicroScopiQ against W416 OliVe for three different LLM benchmarks. MicroScopiQ at lower-precision than OliVe achieves  $\geq 8\%$  **higher accuracy** on the benchmarks compared to OliVe. OliVe shows poor accuracy due to its assumption on outlier locality, resulting in unintended outlier pruning. In Table 4 we also compare MicroScopiQ against OliVe and OmniQuant at W2A16 setting on 4 other LLM benchmarks. MicroScopiQ consistently outperforms all baselines by up to 9% across all benchmarks.

**Effective Bit Width.** For  $bb = 2, 4$ , MicroScopiQ has an EBW of 2.36 and 4.15 bits respectively. Techniques like GOBO, have a very high EBW of 15.6, 18.17 bits. All other baselines employ software-managed metadata and have an  $\text{EBW} = bb$ .

### 6.3 VLM Quantization Results

In Figure 8, we compare 0-shot and multi-shot (4, 8, 16, 32) weight-only quantization performance of OpenFlamingo-9B on the COCO captioning task and VILA-7B on VizWiz, TextVQA benchmarks. At W4A16 quantization, MicroScopiQ consistently outperforms all baselines and achieves on average **less than 1% accuracy drop** compared to the full-precision baseline, demonstrating the flexibility and widespread applicability of our method. Furthermore, at W2A16 quantization, MicroScopiQ achieves high accuracy ( $< 4\%$  accuracy drop), outperforming several W4A16 baselines.

### 6.4 Accelerator Results

**Compute Area.** In Table 5, we compare the accelerator compute area breakdown of MicroScopiQ (w/ 1 ReCoN unit) with baselines GOBO and OliVe for a  $64 \times 64$  array design. For a fair evaluation, all accelerators have identical configurations with same number of PEs. MicroScopiQ has a very low compute overhead 8.63%, compared to OliVe’s 9.90%. This is because, units like ReCoN which perform three simple operations for outlier processing has a very low area utilization compared to OliVe’s encoders and decoders. ReCoN is also time-multiplexed across all rows resulting in minimal area overhead (see §6.5). Furthermore, the simple INT operations of MicroScopiQ allows the packing of more compute power with

**Table 5: Compute area and density comparison for a  $64 \times 64$  array at 7nm process technology.**

Architecture	Component (Area ( $\mu\text{m}^2$ ), # Units)	Compute area ( $\text{mm}^2$ )	Compute overhead	Compute density ( $\text{TOPS}/\text{mm}^2$ )
GOBO [81]	Group PE (36.56, 4096 $\times$ )	0.216	3.28%	28.28
	Outlier PE (96.42, 64 $\times$ )			
	Control unit (115.36, 1 $\times$ )			
OliVe [23]	4-bit Decoder (1.86, 128 $\times$ )	0.011	9.90%	184.30
	8-bit decoder (2.47, 64 $\times$ )			
	Base PE (2.51, 4096 $\times$ )			
	Multi-Precision support (0.68, 1024 $\times$ )			
MicroScopiQ	Control unit (95.49, 1 $\times$ )	0.012	8.63%	367.51
	ReCoN (204.68, 1 $\times$ )			
	Sync buffer (20.45, 1 $\times$ )			
	Base PE (2.82, 4096 $\times$ )			
	Multi-precision support (0.22, 4096 $\times$ )			
	Control unit (105.78, 1 $\times$ )			

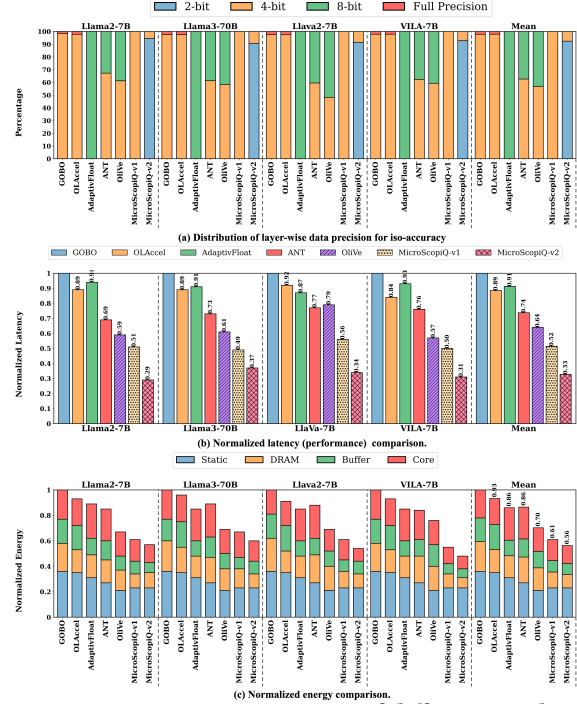


**Figure 9: Iso-accuracy comparison of different accelerators.** MicroScopiQ-v1 and -v2 are executed on the same accelerator and correspond to two different data-precision distributions. minimal overheads. A similar multi-precision design in OliVe would require 3.5-4 $\times$  higher multi-precision support area due to complex exponent-integer PEs. GOBO has an order of magnitude higher compute area compared to OliVe and MicroScopiQ due to large per-PE area.

**Maximum Performance Per Unit Area ( $\text{TOPS}/\text{mm}^2$ ).** We also estimate the peak compute throughput per unit area of each accelerator, using LLaMA3-8B as the workload and report it as the compute density in Table 5. To achieve peak throughput for MicroScopiQ, FMs must be quantized to low precision (e.g.,  $bb = 2$ ). MicroScopiQ **achieves nearly 2 $\times$  and 14 $\times$  higher compute density** than OliVe and GOBO respectively.

**Iso-Accuracy Performance Comparison.** To enable a fair comparison of the latency of different accelerators, we perform an iso-accuracy comparison. We quantize different weight layers of the baseline models using 2-, 4-, or 8-bit precisions, with activations fixed at 8-bit (Figure 9(a)). This ensures all model accuracies are within  $\pm 1\%$  of the best quantized model i.e., W4A8 MicroScopiQ. In Figure 9(b) we compare the normalized latency of baselines against

**Table 6: Effect on Llama3-8B PPL [50] upon progressive inclusion of different quantization techniques.**

Quantization Method	WikiText2 PPL ↓
Baseline W16A16	6.13 (-)
+ Quantize all weights to INT-4	10.27 (↑ 4.14)
+ Quantize all weights to MX-INT-4 <sub>128</sub>	9.53 (↓ 0.74)
+ Quantize all weights to MX-INT-2 <sub>128</sub>	39.48 (↑ 29.95)
+ Quantize outliers to MX-FP-4 <sub>128,128</sub>	10.96 (↓ 28.52)
+ Quantize outliers to MX-FP-4 <sub>8,8</sub>	8.93 (↓ 2.03)
+ Reduce outlier mag. by $\times 2^{L_{sf}}$	8.89 (↓ 0.04)
+ Prune least imp. inliers per $\mu B$	9.02 (↑ 0.13)
+ Compensate quantization errors/rB	8.97 (↓ 0.05)
+ Quantize activations to MX-INT-8 <sub>128</sub> , $\alpha = 0.7$	9.08 (↑ 0.11)
+ 2-bit KV-cache quantization [46]	9.58 (↑ 0.50)

two versions of MicroScopiQ, v1: corresponds to W4A8 quantization with all layers with  $bb = 4$  and v2: most layers quantized such that  $bb = 2$ , with a small percentage of layers with  $bb = 4$  for iso-accuracy. MicroScopiQ v1 and v2 consistently outperform all baselines across models, achieving an **average speedup of 1.50× and 2.47×** respectively. The higher speedup of MicroScopiQ v2 is due to most layers at  $bb = 2$ , allowing the PEs to perform higher throughput low precision computation, compared to  $bb = 4$ . OliVe has most layers quantized to 8-bits, contributing to high latency.

**Iso-Accuracy Energy Comparison.** In Figure 9(c), we show the normalized energy consumption of different accelerators, composed of static and dynamic energy. MicroScopiQ v2 has the lowest energy consumption. Compared to designs like GOBO, OLAcel and AdaptiveFloat, where computations happen at higher-precisions in 8-bit and 32-bit PEs, MicroScopiQ v2 has a significant advantage in terms of the core and DRAM dynamic energy consumption with simple INT PEs. On average MicroScopiQ v2, has **1.5× lower energy consumption** compared to all baselines across different FMs.

## 6.5 Algorithm ablations

**Per-component accuracy impact.** In Table 6 we examine the accuracy gained or lost by progressively incorporating the quantization techniques proposed in MicroScopiQ. We initially adopt INT-4 scalar quantization on the LLaMa3-8B full-precision baseline. We then apply MX-INT-4<sub>128</sub>. However, on decreasing precision to 2-bit INTs i.e., MX-INT-2<sub>128</sub>, we observe a spike in PPL, due to higher outlier quantization error. Upon quantizing outliers to MX-FP-4<sub>8,8</sub>, we regain the lost performance due to preserving outlier values at higher-precision and FP-format. Furthermore, we observe that pruning of least important weights causes a minor increase in PPL, which is regained by Hessian update. We observe that quantizing activations with simple MX-INT-8<sub>128</sub> with a high  $\alpha$  results in a very minimal increase in PPL due to the robustness of MicroScopiQ.

**KV-cache quantization.** In Table 6 we also report the impact of KV-cache quantization on performance. Following the 2-bit KV-cache quantization technique proposed in [46] we quantize K per channel, and the V per token with a MaB of size 128 and residual token length (R) [46] of 128 for both key and value.

**Omni-MicroScopiQ.** Our method is orthogonal to the techniques proposed in OmniQuant. We combine our method with OmniQuant to further improve the quantization performance of MicroScopiQ. We employ OmniQuant’s Learnable Weight Clipping (LWC) to learn both the inlier and outlier scale factors of MicroScopiQ and leverage the Learnable Equivalent Transformation (LET) to learn to migrate the quantization difficulty of activations to weights. In Table 3 we compare the performance of MicroScopiQ enhanced

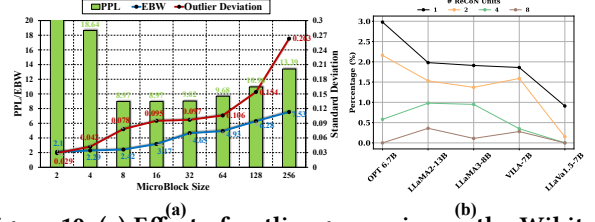


**Figure 10: (a) Effect of outlier group size on the Wikitext-v2 perplexity (PPL) and EBW of a MicroScopiQ quantized LLaMA3-8B.  $\infty$  is per-tensor granularity. (b) Percentage access conflicts to ReCoN for  $64 \times 64$  PE array.**

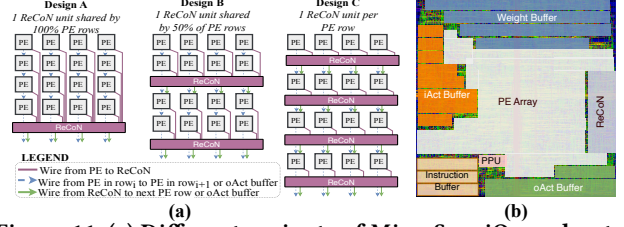


**Figure 11: (a) Different variants of MicroScopiQ accelerator with varying number of ReCoN units. (b) Annotated MicroScopiQ floorplan ( $64 \times 64$  array) with OmniQuant (Omni-MicroScopiQ) against OmniQuant. Omni-MicroScopiQ delivers improvements up to 22%.**

**Outlier group size.** In Figure 10(a), we analyze the effect of different  $B_\mu$  values on outlier diversity (measure by the standard deviation: red line), PPL (green bar), and EBW (blue line) for LLaMa3-8B. For  $B_\mu = 2, 4$ , accuracy degradation occurs due to outlier pruning, as many MBs have  $\geq B_\mu/2$  outliers. As  $B_\mu$  increases, outliers further apart show greater diversity, evidenced by the higher standard deviation. For  $B_\mu \geq 32$ , this results in increased quantization error and higher PPL, as MX-FP scales are shared across more diverse outlier values. Larger group sizes also significantly increase EBW due to metadata overhead. A balance is achieved at  $B_\mu = 8$ .

## 6.6 Analysis of time-multiplexed ReCoN

**Accelerator design variants.** In Figure 11(a), we show the layout of different variants of MicroScopiQ with varying number of ReCoN units, each of which can be employed based on application requirements. For area critical applications, design A, with a single ReCoN can be employed to have minimal area utilization with a slight increase in latency due to access conflicts to ReCoN. With the addition of more ReCoN units, fewer rows of PEs share a single ReCoN, dramatically reducing access conflicts to the shared ReCoN unit (design B). When the number of ReCoN units equals the number of rows, each PE row gets a dedicated ReCoN unit as shown in design C, which can be employed for latency critical applications. As we shall demonstrate subsequently, we identified that in up to a  $128 \times 128$  PE array size, a total of 8 ReCoN units are sufficient to achieve peak performance with zero access conflicts to ReCoN.

**Optimal # of ReCoN units.** For a  $64 \times 64$  MicroScopiQ accelerator, we study the number of access conflicts for different number of ReCoN units in Figure 10(b). Evidently, the number of access conflicts to ReCoN which is measured as the percent of total number of accesses to ReCoN that result in conflicts is under 3%. With the progressive addition of more ReCoN units, the access conflicts tend to 0%. In Figure 9, despite the access conflicts, 1 ReCoN unit is sufficient to reach good inference performance in an iso-accuracy

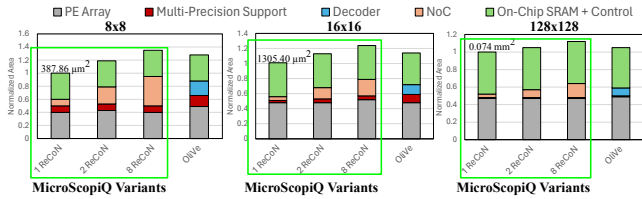


**Figure 12: Comparison of area of MicroScopiQ and OliVe at different PE array sizes. Three different versions of MicroScopiQ are depicted with different number of ReCoN units.**

scenario. For latency critical applications, in Figure 13(a), we quantify the performance improvement and impact on compute area by incorporating multiple ReCoN units for a LLaMA3-8B FM. Up to 8 ReCoN units enables peak performance with **21% improved latency** and only **1.58x higher compute area**. For large array sizes, up to 8 ReCoN units are sufficient for peak performance.

### 6.7 Scalability and Timing Analysis

**Scalability.** To study how MicroScopiQ scales to different PE array sizes, we compare the total area (including on-chip weight and iAct/oAct buffers) against OliVe at three different scales:  $8 \times 8$ ,  $16 \times 16$ ,  $128 \times 128$  in Figure 12. Following [68], for  $8 \times 8$  array we employ 16 kB iAct and oAct buffers and 32 kB weight buffer. We progressively scale the buffers for larger arrays to ensure full array utilization. Since varying the number of ReCoN units trades off area for performance, we also compare three versions of MicroScopiQ with 1, 2, 8 ReCoN units. For the single ReCoN variant of MicroScopiQ, as the design scales to higher array sizes, the area overhead of ReCoN decreases ( $128 \times 128$  has overhead of 3%), with the on-chip area being dominated by the large PE array and buffers. We observe similar trends for 2 or 8 ReCoN units. At large PE array sizes such as  $128 \times 128$ , adding 8 ReCoN units results in a minimal overhead of just 11%. Particularly at large array sizes the column-wise bus from PEs to ReCoN can be routed over logic as the PE array scales. With same buffer configurations, OliVe has a higher area compared to a single ReCoN MicroScopiQ variant, while comparable area to MicroScopiQ with 8 ReCoN units. At all variants, MicroScopiQ has 2 – 3x higher performance than OliVe (see Table 5).

**Timing Analysis.** MicroScopiQ at all scales attains a peak clock frequency of 1 GHz. The critical path for MicroScopiQ is from the local weights registers to multipliers within the PE. The column-wise bus (the longest wire in MicroScopiQ) from PEs to ReCoN is not on the critical path and therefore does not limit scalability<sup>6</sup>.

**Implementation overhead on NoC-based accelerators.** The global column-wise bus is a design commonly seen in AI ASICs like [8, 17, 64, 72]. These global buses are used in conjunction with the NoC in these designs for data distribution, layout reordering [72]. We modify two large-scale accelerators MTIA and Eyeriss-v2 that employ NoCs in their design to support MicroScopiQ, by incorporating ReCoN functionality in the accelerator NoCs and modifying PEs to support all MicroScopiQ specific operations. As shown in Figure 13(b), compared to the baseline design of MTIA and Eyeriss-v2, integrating ReCoN and MicroScopiQ PEs results in only a 3% and 2.3% increase in compute area, respectively. Since

<sup>6</sup>For extremely large arrays, if global wire becomes a bottleneck, it can be resolved by pipelining/adding more ReCoN units (for timing) or laying wires over logic (for area).

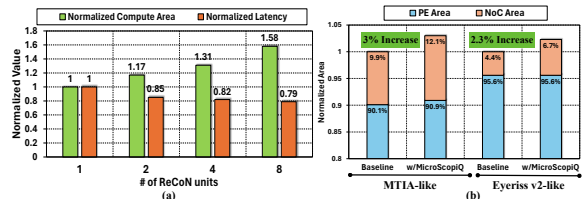


**Figure 13: (a) Effect of time-multiplexed ReCoN units on the compute area and inference latency, (b) Implementation overhead of MicroScopiQ in NoC-based accelerators [8, 17] these designs already employ NoCs, integration overhead of MicroScopiQ is minimal. This demonstrates that the benefits achieved by MicroScopiQ are attained at minimal to no additional cost.**

## 7 Related Work

**Model compression for LLMs.** LLM weight Compression scheme like quantization often rely on mixed-precision quantization with different outlier and inlier bit-widths [14, 28, 31, 39, 85]. For instance, SDQ [31] decomposes a vector of weights into two separate inlier and outlier vectors each quantized at different precisions. Other class of quantization rely on channel-wise shared scaling with different scale factors for outliers [28, 39, 63]. Other quantization techniques mitigate outliers from weights and activations [4, 47, 77] to make quantization easier.

LLM weight pruning methods [3, 18, 80] rely on approximate solvers to identify the importance of weights based on magnitude of weights or weights activation combined [69]. However, they fail to achieve satisfactory performance even at low sparsity levels [48]. *MicroScopiQ provides a unified solution for outlier-aware quantization by enabling flexible pruning of least-important weights to distribute additional outlier bits, thereby, simultaneously achieving high accuracy and hardware efficiency.*

**Accelerator for quantized models.** Accelerators like GOBO [81], OLAccel [53] use high-precision PEs for outliers and low-precision PEs for inliers. OliVe [23] incorporates encoding/decoding units in a PE array for inlier-outlier formats, while other accelerators [24, 59, 71] propose adaptive formats and hybrid FP PEs. However, they often suffer from unaligned memory access and large overheads. *MicroScopiQ accelerator introduces a novel low overhead NoC called ReCoN, that effectively abstracts FP-format complexity from INT-PEs*

**NoCs in ML Accelerators.** NoCs are widely used in accelerators: [51, 57] employ a Benes NoC for data distribution, [72] uses a butterfly NoC for layout transformation, and [8, 17] utilize mesh NoCs. *ReCoN is a butterfly NoC employed to compute FP partial sums.*

## 8 Conclusion

In this paper, we introduce MicroScopiQ, a novel co-design technique for post-training quantization of FMs. MicroScopiQ addresses outlier-aware quantization by: a) using higher-precision MX-FP for outliers and lower-precision INTs for inliers to maintain accuracy, and b) pruning to distribute additional outlier bits, ensuring memory alignment and hardware efficiency. The MicroScopiQ accelerator, featuring multi-precision PEs and a ReCoN NoC, efficiently handles distributed outliers. MicroScopiQ is the first PTQ technique to achieve SoTA compression for both LLMs and VLMs at just 2.36-bits, offering 3x better inference performance and 2x lower energy consumption than existing accelerators.

## References

- [1] Marah Abdin, Sam Ade Jacobs, Ammar Ahmad Awan, Jyoti Aneja, Ahmed Awadallah, Hany Awadalla, Nguyen Bach, Amit Bahree, Arash Bakhtiari, Harkirat Behl, et al. 2024. Phi-3 technical report: A highly capable language model locally on your phone. *arXiv preprint arXiv:2404.14219* (2024).
- [2] Jean-Baptiste Alayrac, Jeff Donahue, Pauline Luc, Antoine Miech, Iain Barr, Yana Hasson, Karel Lenc, Arthur Mensch, Katherine Millican, Malcolm Reynolds, et al. 2022. Flamingo: a visual language model for few-shot learning. *Advances in neural information processing systems* 35 (2022), 23716–23736.
- [3] Saleh Ashkboos, Maximilian L Croci, Marcelo Gennari do Nascimento, Torsten Hoefler, and James Hensman. 2024. Sliceqpt: Compress large language models by deleting rows and columns. *arXiv preprint arXiv:2401.15024* (2024).
- [4] Saleh Ashkboos, Amirkeivan Mohtashami, Maximilian L Croci, Bo Li, Martin Jaggi, Dan Alistarh, Torsten Hoefler, and James Hensman. 2024. Quarot: Outlier-free 4-bit inference in rotated llms. *arXiv preprint arXiv:2404.00456* (2024).
- [5] Anas Awadalla, Irena Gao, Josh Gardner, Jack Hessel, Yusuf Hanafy, Wanrong Zhu, Kalyani Marathe, Yonatan Bitton, Samir Gadre, Shiori Sagawa, et al. 2023. Openflamingo: An open-source framework for training large autoregressive vision-language models. *arXiv preprint arXiv:2308.01390* (2023).
- [6] Yonatan Bisk, Rowan Zellers, Jianfeng Gao, Yejin Choi, et al. 2020. Piqa: Reasoning about physical commonsense in natural language. In *Proceedings of the AAAI conference on artificial intelligence*, Vol. 34. 7432–7439.
- [7] Xinlei Chen, Hao Fang, Tsung-Yi Lin, Ramakrishna Vedantam, Saurabh Gupta, Piotr Dollár, and C Lawrence Zitnick. 2015. Microsoft coco captions: Data collection and evaluation server. *arXiv preprint arXiv:1504.00325* (2015).
- [8] Yu-Hsin Chen, Tien-Ju Yang, Joel Emer, and Vivienne Sze. 2019. Eyeriss v2: A flexible accelerator for emerging deep neural networks on mobile devices. *IEEE Journal on Emerging and Selected Topics in Circuits and Systems* 9, 2 (2019), 292–308.
- [9] Christopher Clark, Kenton Lee, Ming-Wei Chang, Tom Kwiatkowski, Michael Collins, and Kristina Toutanova. 2019. BoolQ: Exploring the surprising difficulty of natural yes/no questions. *arXiv preprint arXiv:1905.10044* (2019).
- [10] Peter Clark, Isaac Cowhey, Oren Etzioni, Tushar Khot, Ashish Sabharwal, Carissa Schoenick, and Oyvind Tafjord. 2018. Think you have solved question answering? try arc, the ai2 reasoning challenge. *arXiv preprint arXiv:1803.05457* (2018).
- [11] Steve Dai, Rangha Venkatesan, Mark Ren, Brian Zimmer, William Dally, and Brucek Kshailany. 2021. Vs-quant: Per-vector scaled quantization for accurate low-precision neural network inference. *Proceedings of Machine Learning and Systems* 3 (2021), 873–884.
- [12] Bitu Darvish Rouhani, Ritchie Zhao, Venmugil Elango, Rasoul Shafiqpour, Mathew Hall, Maral Mesmakhoshroshahi, Ankit More, Levi Melnick, Maximilian Golub, Girish Varatkar, et al. 2023. With shared microexponents, a little shifting goes a long way. In *Proceedings of the 50th Annual International Symposium on Computer Architecture*. 1–13.
- [13] Tim Dettmers, Mike Lewis, Younes Belkada, and Luke Zettlemoyer. 2022. LLM.int8 () 8-bit matrix multiplication for transformers at scale. In *Proceedings of the 36th International Conference on Neural Information Processing Systems*. 30318–30332.
- [14] Tim Dettmers, Ruslan Svirschevski, Vage Egiazarian, Denis Kuznedelev, Elias Frantar, Saleh Ashkboos, Alexander Borzunov, Torsten Hoefler, and Dan Alistarh. 2023. Spqr: A sparse-quantized representation for near-lossless llm weight compression. *arXiv preprint arXiv:2306.03078* (2023).
- [15] Jacob Devlin, Ming-Wei Chang, Kenton Lee, and Kristina Toutanova. 2018. Bert: Pre-training of deep bidirectional transformers for language understanding. *arXiv preprint arXiv:1810.04805* (2018).
- [16] Mario Drummond, Tao Lin, Martin Jaggi, and Babak Falsafi. 2018. Training dnns with hybrid block floating point. *Advances in Neural Information Processing Systems* 31 (2018).
- [17] Amin Firoozshahian, Joel Coburn, Roman Levenstein, Rakesh Nattoji, Ashwin Kamath, Olivia Wu, Gurdeepak Grewal, Harish Aepala, Bhasker Jakka, Bob Dreyer, et al. 2023. Mtia: First generation silicon targeting meta’s recommendation systems. In *Proceedings of the 50th Annual International Symposium on Computer Architecture*. 1–13.
- [18] Elias Frantar and Dan Alistarh. 2023. Sparsegpt: Massive language models can be accurately pruned in one-shot. In *International Conference on Machine Learning*. PMLR, 10323–10337.
- [19] Elias Frantar, Saleh Ashkboos, Torsten Hoefler, and Dan Alistarh. 2022. Gptq: Accurate post-training quantization for generative pre-trained transformers. *arXiv preprint arXiv:2210.17323* (2022).
- [20] Leo Gao, Stella Biderman, Sid Black, Laurence Golding, Travis Hoppe, Charles Foster, Jason Phang, Horace He, Anish Thite, Noa Nabeshima, et al. 2020. The pile: An 800gb dataset of diverse text for language modeling. *arXiv preprint arXiv:2101.00027* (2020).
- [21] Ian Goodfellow, Jean Pouget-Abadie, Mehdi Mirza, Bing Xu, David Warde-Farley, Sherjil Ozair, Aaron Courville, and Yoshua Bengio. 2014. Generative adversarial nets. *Advances in neural information processing systems* 27 (2014).
- [22] Yash Goyal, Tejas Khot, Douglas Summers-Stay, Dhruv Batra, and Devi Parikh. 2017. Making the v in vqa matter: Elevating the role of image understanding in visual question answering. In *Proceedings of the IEEE conference on computer vision and pattern recognition*. 6904–6913.
- [23] Cong Guo, Jiaming Tang, Weiming Hu, Jingwen Leng, Chen Zhang, Fan Yang, Yunxin Liu, Minyi Guo, and Yuhao Zhu. 2023. Olive: Accelerating large language models via hardware-friendly outlier-victim pair quantization. In *Proceedings of the 50th Annual International Symposium on Computer Architecture*. 1–15.
- [24] Cong Guo, Chen Zhang, Jingwen Leng, Zihan Liu, Fan Yang, Yunxin Liu, Minyi Guo, and Yuhao Zhu. 2022. Ant: Exploiting adaptive numerical data type for low-bit deep neural network quantization. In *2022 55th IEEE/ACM International Symposium on Microarchitecture (MICRO)*. IEEE, 1414–1433.
- [25] Danna Gurari, Qing Li, Abigale J Stangl, Anhong Guo, Chi Lin, Kristen Grauman, Jiebo Luo, and Jeffrey P Bigham. 2018. Vizviz grand challenge: Answering visual questions from blind people. In *Proceedings of the IEEE conference on computer vision and pattern recognition*. 3608–3617.
- [26] Babak Hassibi, David G Stork, and Gregory J Wolff. 1993. Optimal brain surgeon and general network pruning. In *IEEE international conference on neural networks*. IEEE, 293–299.
- [27] Dan Hendrycks, Collin Burns, Steven Basart, Andy Zou, Mantas Mazeika, Dawn Song, and Jacob Steinhardt. 2020. Measuring massive multitask language understanding. *arXiv preprint arXiv:2009.03300* (2020).
- [28] Wei Huang, Xudong Ma, Haotong Qin, Xingyu Zheng, Chengtao Lv, Hong Chen, Jie Luo, Xiaojuan Qi, Xianglong Liu, and Michele Magno. 2024. How good are low-bit quantized llama3 models? an empirical study. *arXiv preprint arXiv:2404.14047* (2024).
- [29] Drew A Hudson and Christopher D Manning. 2019. Gqa: A new dataset for real-world visual reasoning and compositional question answering. In *Proceedings of the IEEE/CVF conference on computer vision and pattern recognition*. 6700–6709.
- [30] Geonhwa Jeong, Sana Damani, Abhimanyu Rajeshkumar Bambhaniya, Eric Qin, Christopher J Hughes, Sreenivas Subramoney, Hyesoon Kim, and Tushar Krishna. 2023. Vegeta: Vertically-integrated extensions for sparse/dense gemm tile acceleration on cpus. In *2023 IEEE International Symposium on High-Performance Computer Architecture (HPCA)*. IEEE, 259–272.
- [31] Geonhwa Jeong, Po-An Tsai, Stephen W Keckler, and Tushar Krishna. 2024. SDQ: Sparse Decomposed Quantization for LLM Inference. *arXiv preprint arXiv:2406.13868* (2024).
- [32] Albert Q Jiang, Alexandre Sablayrolles, Antoine Roux, Arthur Mensch, Blanche Savary, Chris Bamford, Devendra Singh Chaitot, Diego de las Casas, Emma Bou Hanna, Florian Bressand, et al. 2024. Mixtral of experts. *arXiv preprint arXiv:2401.04088* (2024).
- [33] Norman P Jouppi, Cliff Young, Nishant Patil, David Patterson, Gaurav Agrawal, Raminder Bajwa, Sarah Bates, Suresh Bhatia, Nan Boden, Al Borchers, et al. 2017. In-datacenter performance analysis of a tensor processing unit. In *Proceedings of the 44th annual international symposium on computer architecture*. 1–12.
- [34] Hao Kang, Qingru Zhang, Souvik Kundu, Geonhwa Jeong, Zaoxing Liu, Tushar Krishna, and Tuo Zhao. 2024. Gear: An efficient kv cache compression recipe for near-lossless generative inference of llm. *arXiv preprint arXiv:2403.05527* (2024).
- [35] Ben Keller, Rangharajan Venkatesan, Steve Dai, Stephen G Tell, Brian Zimmer, Charbel Sakr, William J Dally, C Thomas Gray, and Brucek Kshailany. 2023. A 95.6-TOPS/W deep learning inference accelerator with per-vector scaled 4-bit quantization in 5 nm. *IEEE Journal of Solid-State Circuits* 58, 4 (2023), 1129–1141.
- [36] Tushar Krishna, Chia-Hsin Owen Chen, Woo-Cheol Kwon, and Li-Shiuan Peh. 2014. Smart: Single-cycle multihop traversals over a shared network on chip. *IEEE micro* 34, 3 (2014), 43–56.
- [37] Andrey Kuzmin, Markus Nagel, Mart Van Baalen, Arash Behboodi, and Tijmen Blankevoort. 2024. Pruning vs quantization: which is better? *Advances in neural information processing systems* 36 (2024).
- [38] Yann LeCun, John Denker, and Sara Solla. 1989. Optimal brain damage. *Advances in neural information processing systems* 2 (1989).
- [39] Changhun Lee, Jungyu Jin, Taesu Kim, Hyungjun Kim, and Eunhyeok Park. 2024. Owq: Outlier-aware weight quantization for efficient fine-tuning and inference of large language models. In *Proceedings of the AAAI Conference on Artificial Intelligence*, Vol. 38. 13355–13364.
- [40] Muyang Li, Ji Lin, Chenlin Meng, Stefano Ermon, Song Han, and Jun-Yan Zhu. 2022. Efficient spatially sparse inference for conditional gans and diffusion models. *Advances in neural information processing systems* 35 (2022), 28858–28873.
- [41] Yuhang Li, Ruihao Gong, Xu Tan, Yang Yang, Peng Hu, Qi Zhang, Fengwei Yu, Wei Wang, and Shi Gu. 2021. Breq: Pushing the limit of post-training quantization by block reconstruction. *arXiv preprint arXiv:2102.05426* (2021).
- [42] Ji Lin, Jiaming Tang, Haotian Tang, Shang Yang, Wei-Ming Chen, Wei-Chen Wang, Guangxuan Xiao, Xingyu Dang, Chuang Gan, and Song Han. 2024. AWQ: Activation-aware Weight Quantization for On-Device LLM Compression and Acceleration. *Proceedings of Machine Learning and Systems* 6 (2024), 87–100.
- [43] Ji Lin, Hongxu Yin, Wei Ping, Pavlo Molchanov, Mohammad Shoeybi, and Song Han. 2024. Vila: On pre-training for visual language models. In *Proceedings of the IEEE/CVF Conference on Computer Vision and Pattern Recognition*. 26689–26699.

- [44] Haotian Liu, Chunyuan Li, Qingyang Wu, and Yong Jae Lee. 2024. Visual instruction tuning. *Advances in neural information processing systems* 36 (2024).
- [45] Yuhao Liu, Shubham Rai, Salim Ullah, and Akash Kumar. 2023. High Flexibility Designs of Quantized Runtime Reconfigurable Multi-Precision Multipliers. *IEEE Embedded Systems Letters* (2023).
- [46] Zirui Liu, Jiayi Yuan, Hongye Jin, Shaochen Zhong, Zhaozhuo Xu, Vladimir Braverman, Beidi Chen, and Xia Hu. 2024. Kivi: A tuning-free asymmetric 2bit quantization for kv cache. *arXiv preprint arXiv:2402.02750* (2024).
- [47] Zechun Liu, Changsheng Zhao, Igor Fedorov, Bilge Soran, Dhruv Choudhary, Raghuraman Krishnamoorthi, Vikas Chandra, Yuandong Tian, and Tijmen Blankevoort. 2024. SpinQuant-LLM quantization with learned rotations. *arXiv preprint arXiv:2405.16406* (2024).
- [48] Xudong Lu, Aojun Zhou, Yuhui Xu, Renrui Zhang, Peng Gao, and Hongsheng Li. 2024. SPP: Sparsity-Preserved Parameter-Efficient Fine-Tuning for Large Language Models. *arXiv preprint arXiv:2405.16057* (2024).
- [49] Stephen Merity, Caiming Xiong, James Bradbury, and Richard Socher. 2016. Pointer sentinel mixture models. *arXiv preprint arXiv:1609.07843* (2016).
- [50] AI Meta. 2024. Introducing meta llama 3: The most capable openly available llm to date. *Meta AI* (2024).
- [51] Francisco Muñoz-Martínez, Raveesh Garg, Michael Pellauer, José L Abellán, Manuel E Acacio, and Tushar Krishna. 2023. Flexagon: A multi-dataflow sparse-sparse matrix multiplication accelerator for efficient dnn processing. In *Proceedings of the 28th ACM International Conference on Architectural Support for Programming Languages and Operating Systems, Volume 3*. 252–265.
- [52] Naveen Muralimanohar, Rajeev Balasubramonian, and Norman P Jouppi. 2009. CACTI 6.0: A tool to model large caches. *HP laboratories 27* (2009), 28.
- [53] Eunhyeok Park, Dongyoung Kim, and Sungjoo Yoo. 2018. Energy-efficient neural network accelerator based on outlier-aware low-precision computation. In *2018 ACM/IEEE 45th Annual International Symposium on Computer Architecture (ISCA)*. IEEE, 688–698.
- [54] Adam Paszke, Sam Gross, Francisco Massa, Adam Lerer, James Bradbury, Gregory Chanan, Trevor Killeen, Zeming Lin, Natalia Gimelshein, Luca Antiga, et al. 2019. Pytorch: An imperative style, high-performance deep learning library. *Advances in neural information processing systems* 32 (2019).
- [55] Open Compute Project. 2024. OCP Microscaling Formats MX V1.0 Spec. <https://www.opencompute.org/documents/ocp-microscaling-formats-mx-v1-0-spec-final-pdf#page=10.23> Accessed: 2024-07-13.
- [56] Friedrich Pukelsheim. 1994. The three sigma rule. *The American Statistician* 48, 2 (1994), 88–91.
- [57] Eric Qin, Ananda Samajdar, Hyoukjun Kwon, Vineet Nadella, Sudarshan Sriniwasan, Dipankar Das, Bharat Kaul, and Tushar Krishna. 2020. Sigma: A sparse and irregular gemm accelerator with flexible interconnects for dnn training. In *2020 IEEE International Symposium on High Performance Computer Architecture (HPCA)*. IEEE, 58–70.
- [58] Akshat Ramachandran, Souvik Kundu, and Tushar Krishna. 2024. CLAMP-ViT: Contrastive Data-Free Learning for Adaptive Post-Training Quantization of ViTs. *arXiv preprint arXiv:2407.05266* (2024).
- [59] Akshat Ramachandran, Zishen Wan, Geonhwa Jeong, John Gustafson, and Tushar Krishna. 2024. Algorithm-Hardware Co-Design of Distribution-Aware Logarithmic-Posit Encodings for Efficient DNN Inference. *arXiv preprint arXiv:2403.05465* (2024).
- [60] Bitu Darvish Rouhani, Ritchie Zhao, Ankit More, Mathew Hall, Alireza Khodamoradi, Summer Deng, Dhruv Choudhary, Marius Cornea, Eric Dellinger, Kristof Denolf, et al. 2023. Microscaling data formats for deep learning. *arXiv preprint arXiv:2310.10537* (2023).
- [61] Keisuke Sakaguchi, Ronan Le Bras, Chandra Bhagavatula, and Yejin Choi. 2021. Winogrande: An adversarial winograd schema challenge at scale. *Commun. ACM* 64, 9 (2021), 99–106.
- [62] Satyabrata Sarangi and Bevan Baas. 2021. DeepScaleTool: A tool for the accurate estimation of technology scaling in the deep-submicron era. In *2021 IEEE International Symposium on Circuits and Systems (ISCAS)*. IEEE, 1–5.
- [63] Wenqi Shao, Mengzhao Chen, Zhaoyang Zhang, Peng Xu, Lirui Zhao, Zhiqian Li, Kaipeng Zhang, Peng Gao, Yu Qiao, and Ping Luo. 2023. Omniquant: Omnidirectionally calibrated quantization for large language models. *arXiv:2308.13137* (2023).
- [64] Yakun Sophia Shao, Jason Clemons, Rangharajan Venkatesan, Brian Zimmer, Matthew Fojtik, Nan Jiang, Ben Keller, Alicia Klinefelter, Nathaniel Pinckney, Priyanka Raina, et al. 2019. Simba: Scaling deep-learning inference with multi-chip-module-based architecture. In *Proceedings of the 52nd Annual IEEE/ACM International Symposium on Microarchitecture*. 14–27.
- [65] Hardik Sharma, Jongse Park, Divya Mahajan, Emmanuel Amaro, Joon Kyung Kim, Chenkai Shao, Asit Mishra, and Hadi Esmaeilzadeh. 2016. From high-level deep neural models to FPGAs. In *2016 49th Annual IEEE/ACM International Symposium on Microarchitecture (MICRO)*. IEEE, 1–12.
- [66] Hardik Sharma, Jongse Park, Naveen Suda, Liangzhen Lai, Benson Chau, Joon Kyung Kim, Vikas Chandra, and Hadi Esmaeilzadeh. 2018. Bit fusion: Bit-level dynamically composable architecture for accelerating deep neural network. In *2018 ACM/IEEE 45th Annual International Symposium on Computer Architecture (ISCA)*. IEEE, 764–775.
- [67] Amanpreet Singh, Vivek Natarajan, Meet Shah, Yu Jiang, Xinlei Chen, Dhruv Batra, Devi Parikh, and Marcus Rohrbach. 2019. Towards vqa models that can read. In *Proceedings of the IEEE/CVF conference on computer vision and pattern recognition*. 8317–8326.
- [68] H Ekin Sumbul, Tony F Wu, Yuecheng Li, Syed Shakib Sarwar, William Koven, Eli Murphy-Trotzky, Xingxing Cai, Elnaz Ansari, Daniel H Morris, Huichu Liu, et al. 2022. System-level design and integration of a prototype AR/VR hardware featuring a custom low-power DNN accelerator chip in 7nm technology for codec avatars. In *2022 IEEE Custom Integrated Circuits Conference (CICC)*. IEEE, 01–08.
- [69] Mingjie Sun, Zhuang Liu, Anna Bair, and J Zico Kolter. 2023. A simple and effective pruning approach for large language models. *arXiv preprint arXiv:2306.11695* (2023).
- [70] Wei Sun, Aojun Zhou, Sander Stuijk, Rob Wijnhoven, Andrew O Nelson, Henk Corporaal, et al. 2021. DominoSearch: Find layer-wise fine-grained N: M sparse schemes from dense neural networks. *Advances in neural information processing systems* 34 (2021), 20721–20732.
- [71] Thierry Tambe, En-Yu Yang, Zishen Wan, Yuntian Deng, Vijay Janapa Reddi, Alexander Rush, David Brooks, and Gu-Yeon Wei. 2020. Algorithm-hardware co-design of adaptive floating-point encodings for resilient deep learning inference. In *2020 57th ACM/IEEE Design Automation Conference (DAC)*. IEEE, 1–6.
- [72] Jianming Tong, Anirudh Itagi, Prasanth Chatarasi, and Tushar Krishna. 2024. FEATHER: A Reconfigurable Accelerator with Data Reordering Support for Low-Cost On-Chip Dataflow Switching. *arXiv preprint arXiv:2405.13170* (2024).
- [73] Hugo Touvron, Louis Martin, Kevin Stone, Peter Albert, Amjad Almahairi, Yasmine Babaei, Nikolay Bashlykov, Soumya Batra, Prajwal Bhargava, Shriti Bhosale, et al. 2023. Llama 2: Open foundation and fine-tuned chat models. *arXiv preprint arXiv:2307.09288* (2023).
- [74] Yaman Umuroglu, Lahiru Rasnayake, and Magnus Sjalander. 2018. Bismo: A scalable bit-serial matrix multiplication overlay for reconfigurable computing. In *2018 28th International Conference on Field Programmable Logic and Applications (FPL)*. IEEE, 307–3077.
- [75] Naigang Wang, Jungwook Choi, Daniel Brand, Chia-Yu Chen, and Kailash Gopalakrishnan. 2018. Training deep neural networks with 8-bit floating point numbers. *Advances in neural information processing systems* 31 (2018).
- [76] Xiaoxia Wu, Haojun Xia, Stephen Youn, Zhen Zheng, Shiyang Chen, Arash Bakhtiari, Michael Wyatt, Yuxiong He, Olatunji Ruwase, Leon Song, et al. 2023. Zeroquant (4+ 2): Redefining llms quantization with a new fp6-centric strategy for diverse generative tasks. *arXiv preprint arXiv:2312.08583* (2023).
- [77] Guangxuan Xiao, Ji Lin, Mickael Seznec, Hao Wu, Julien Demouth, and Song Han. 2023. Smoothquant: Accurate and efficient post-training quantization for large language models. In *International Conference on Machine Learning*. PMLR, 38087–38099.
- [78] Jingfeng Yang, Hongye Jin, Ruixiang Tang, Xiaotian Han, Qizhang Feng, Haoming Jiang, Shaochen Zhong, Bing Yin, and Xia Hu. 2024. Harnessing the power of llms in practice: A survey on chatgpt and beyond. *ACM Transactions on Knowledge Discovery from Data* 18, 6 (2024), 1–32.
- [79] Lu Yin, AJAY KUMAR JAISWAL, Shiwei Liu, Souvik Kundu, and Zhangyang Wang. [n. d.]. Junk DNA Hypothesis: Pruning Small Pre-Trained Weights Irreversibly and Monotonically Impairs “Difficult” Downstream Tasks in LLMs. In *Forty-first International Conference on Machine Learning*.
- [80] Lu Yin, You Wu, Zhenyu Zhang, Cheng-Yu Hsieh, Yaqing Wang, Yiling Jia, Mykola Pechenizkiy, Yi Liang, Zhangyang Wang, and Shiwei Liu. 2023. Outlier weighed layerwise sparsity (owl): A missing secret sauce for pruning llms to high sparsity. *arXiv preprint arXiv:2310.05175* (2023).
- [81] Ali Hadi Zadeh, Isak Edo, Omar Mohamed Awad, and Andreas Moshovos. 2020. Gobo: Quantizing attention-based nlp models for low latency and energy efficient inference. In *2020 53rd Annual IEEE/ACM International Symposium on Microarchitecture (MICRO)*. IEEE, 811–824.
- [82] Rowan Zellers, Ari Holtzman, Yonatan Bisk, Ali Farhadi, and Yejin Choi. 2019. Hellaswag: Can a machine really finish your sentence? *arXiv preprint arXiv:1905.07830* (2019).
- [83] Biao Zhang, Zhongtao Liu, Colin Cherry, and Orhan Firat. 2024. When scaling meets llm finetuning: The effect of data, model and finetuning method. *arXiv preprint arXiv:2402.17193* (2024).
- [84] Susan Zhang, Stephen Roller, Naman Goyal, Mikel Artetxe, Moya Chen, Shuohui Chen, Christopher Dewan, Mona Diab, Xian Li, Xi Victoria Lin, et al. 2022. Opt: Open pre-trained transformer language models. *arXiv preprint arXiv:2205.01068* (2022).
- [85] Yilong Zhao, Chien-Yu Lin, Kan Zhu, Zihao Ye, Lequn Chen, Size Zheng, Luis Ceze, Arvind Krishnamurthy, Tianqi Chen, and Baris Kasikci. 2024. Atom: Low-bit quantization for efficient and accurate llm serving. *Proceedings of Machine Learning and Systems* 6 (2024), 196–209.